

3 σ Nonlinear Isotope Shift in Yb⁺ Search for New Boson

Ian Counts,^{1,*} Joonseok Hur,^{1,*} Diana P. L. Aude Craik,¹ Honggi Jeon,² Calvin Leung,¹ Julian C. Berengut,³ Amy Geddes,³ Akio Kawasaki,⁴ Wonho Jhe,² and Vladan Vuletić^{1,†}

¹Department of Physics and Research Laboratory of Electronics,

Massachusetts Institute of Technology, Cambridge, Massachusetts 02139, USA

²Department of Physics and Astronomy, Seoul National University, Seoul 151-747, Korea

³School of Physics, University of New South Wales, Sydney, New South Wales 2052, Australia

⁴W. W. Hansen Experimental Physics Laboratory and Department of Physics,
Stanford University, Stanford, California 94305, USA

We measure isotope shifts for five Yb⁺ isotopes with zero nuclear spin on two narrow optical quadrupole transitions $^2S_{1/2} \rightarrow ^2D_{3/2}$, $^2S_{1/2} \rightarrow ^2D_{5/2}$ with an accuracy of ~ 300 Hz. The corresponding King plot shows a 3×10^{-7} deviation from linearity at the 3σ uncertainty level. Such a nonlinearity can indicate physics beyond the Standard Model (SM) in the form of a new bosonic force carrier, or arise from higher-order nuclear effects within the SM. We identify the quadratic field shift as a possible nuclear contributor to the nonlinearity at the observed scale, and show how the nonlinearity pattern can be used in future, more accurate measurements to separate a new-boson signal from nuclear effects.

The Standard Model (SM) of particle physics describes virtually all measurements of elementary particles exquisitely well, and yet various indirect evidence points to physics beyond the SM. This evidence includes the preponderance of dark matter of unknown composition in our universe, astronomically observed with several different methodologies such as the rotation curves of galaxies [1], the motion of colliding galaxy clusters [2], gravitational lensing [3], and the power spectrum of the cosmic microwave background [4]. Physics beyond the SM is also being probed in various laboratory experiments, such as high-energy collisions [5], searches for weakly interacting massive particles [5], axions, and axion-like particles [6], precision measurements of the electric dipole moments of elementary particles [7], and other precision tests [8].

Dark-matter candidates can be characterized by their mass, spin, and interactions. In the intermediate mass range from ~ 100 eV/ c^2 to ~ 100 MeV/ c^2 , a new method

has been proposed to search for a dark-matter boson ϕ that couples to quarks and leptons [9, 10]. The virtual exchange of ϕ between neutrons and electrons in an atom would result in a Yukawa-like potential in addition to the Coulomb potential of the nucleus (see Fig. 1). The corresponding shift in energy levels and transition frequencies is too small to be detected by directly comparing spectroscopic data to (much less accurate) atomic-structure calculations, but could potentially be detected through precision isotope shift measurements [11–14] that allow one to sidestep electronic-structure calculations. In particular, the scaled isotope shifts on two different transitions exhibit a linear relationship (King plot [15]), and Refs. [9, 10] argue that a deviation from linearity can indicate a new force mediator ϕ . Such studies are particularly timely as recent experiments analyzing nuclear decay in ^8Be and ^4He have observed a 7σ deviation from the SM [16–18] that could be potentially explained by a new boson with a mass of 17 MeV/ c^2 ($X17$ boson) [19–22]. According to Ref. [10], measurements of optical transitions with a resolution of 1 Hz in select atomic systems could probe this scenario. However, higher-order effects within the SM can result in nonlinearities that limit the sensitivity to new physics [23–26].

In this Letter, we report a precision measurement of the isotope shift for five isotopes of Yb⁺ ions with zero nuclear spin on two narrow optical quadrupole transitions ($^2S_{1/2} \rightarrow ^2D_{3/2}$, $^2S_{1/2} \rightarrow ^2D_{5/2}$) with an accuracy of ~ 300 Hz. Displaying the data in a King plot [15], we observe a deviation from linearity at the 10^{-7} level, corresponding to 3 standard deviations σ . With four independent isotope-shift data points available, we further introduce a novel parametrization of the nonlinearity pattern that can be used to distinguish between nonlinearities of the same magnitude but different physical origin. At the current level of precision, the observed nonlinearity pattern is consistent with both a new boson, and the quadratic

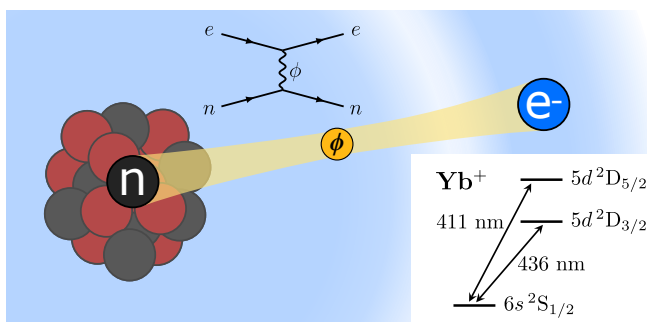


FIG. 1. New intra-atomic force between electron (e^-) and neutron (n) mediated by the virtual exchange of a hypothetical new boson ϕ . The coupling results in a Yukawa-like potential that modifies the atomic energy levels, and can be probed with isotope shift spectroscopy. We perform precision measurements of the long-lived states $^2D_{3/2}$, $^2D_{5/2}$ on individual trapped Yb⁺ ions.

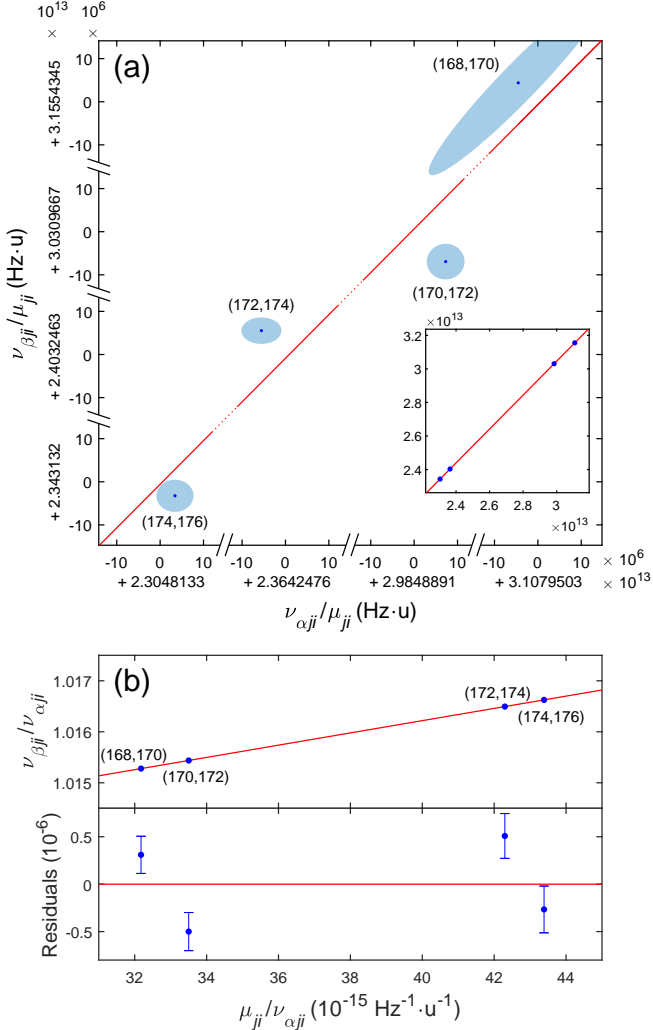


FIG. 2. (a) Standard King plot (Eq. 2) for the $\alpha = 411$ nm, $^2S_{1/2} \rightarrow ^2D_{5/2}$, and $\beta = 436$ nm, $^2S_{1/2} \rightarrow ^2D_{3/2}$ transitions for next-neighbor pairs of even Yb⁺ isotopes. The main figure is zoomed into the data points by a factor of 10^6 . A deviation from linearity (red line) by 3 standard deviations σ is observed. The larger diagonal uncertainty for the (168, 170) pair is due to the larger mass uncertainty for the ¹⁶⁸Yb⁺ isotope [30–32] (see SMat [33]). (b) Frequency-normalized King plot (Eq. 3) and residuals. The error bars and error ellipses indicate 1σ .

field shift (QFS) [23] that we identify as the leading source of nonlinearity within the SM by means of precision electronic-structure calculations. In the future, more accurate measurements on the present and other optical transitions in Yb and Yb⁺ [27–29] can discriminate between effects within and outside the SM.

Our measurements are performed with individual ^{*j*}Yb⁺ ions ($j \in \{168, 170, 172, 174, 176\}$) trapped in a linear Paul trap, and Doppler cooled on the $6s\ ^2S_{1/2} \rightarrow 6p\ ^2P_{1/2}$ transition to typically 500 μ K [35]. We perform optical precision spectroscopy on the transitions

to two long-lived excited states (with electron configurations $[\text{Xe}]4f^{14}6s\ ^2S_{1/2} \rightarrow [\text{Xe}]4f^{14}5d^2D_{3/2}, ^2D_{5/2}$) using light at the wavelengths 411 nm and 436 nm, respectively. The probe light is generated by a frequency-doubled Ti:Sapphire laser that is frequency stabilized to an ultralow-thermal-expansion cavity, achieving a short-term stability of ~ 200 Hz. Typically 1 mW of 411-nm light (0.2 mW of 436-nm light) are focused to a waist of $w_0 = 60 \mu\text{m}$ ($w_0 = 15 \mu\text{m}$) at the location of the ion (see Supplemental Material (SMat) [33] for details).

Coherent optical Ramsey spectroscopy is carried out with two $\frac{\pi}{2}$ pulses of 411-nm or 436-nm light, lasting 5 μs each, separated by 10 μs . This is followed by readout of the state, performed using an electron-shelving scheme [36] (see SMat [33]). A small magnetic field of typically ~ 1.1 G is applied to separate the different Zeeman components of the $S \rightarrow D$ transition. Frequency scans are taken over the central Ramsey fringes of the two symmetric Zeeman components with the lowest magnetic-field sensitivity to find the center frequency of the transition (see SMat [33]).

The measurement on one isotope is averaged typically for 30 minutes before we switch to a next-neighboring isotope by adjusting the various loading, cooling, and repumper laser frequencies. We typically perform three interleaved measurements of each isotope to determine an isotope shift, allowing us to reach a precision on the order of ~ 300 Hz (see Table I and Fig. 2), limited mainly by drifts in the frequency stabilization of the probe laser to the ultrastable cavity (see SMat [33]).

The frequency shift $\nu_{\alpha ji}$ between isotope ^{*j*}Yb and ^{*i*}Yb on an optical transition α can be written as a sum of terms that factorize into a nuclear part (with subscript ji) and an electronic part (with subscript α) [9, 15, 24]

$$\nu_{\alpha ji} = F_\alpha \delta \langle r^2 \rangle_{ji} + K_\alpha \mu_{ji} + G_\alpha [\delta \langle r^2 \rangle_{ji}^2] + v_{ne} D_\alpha a_{ji} \quad (1)$$

Here $\delta \langle r^2 \rangle_{ji} \equiv \langle r^2 \rangle_j - \langle r^2 \rangle_i$ is the difference in squared charge radii r between isotope j and i , $\mu_{ji} \equiv 1/m_j - 1/m_i$ is the inverse-mass difference, $[\delta \langle r^2 \rangle_{ji}^2] \equiv (\delta \langle r^2 \rangle_{jl})^2 - (\delta \langle r^2 \rangle_{il})^2$ for some fixed isotope l (the choice of l is irrelevant to the nonlinearity; see SMat [33]), and $a_{ji} = j - i$ is the difference in neutron number. The quantity $v_{ne} = (-1)^{s+1} y_n y_e / (4\pi\hbar c)$ is the product of the coupling factors of the new boson to the neutron y_n and electron y_e , creating a Yukawa-like potential given by $V_{ne}(r) = \hbar v_{ne} \exp(-r/\lambda_c)/r$ for a boson with spin s , mass m_ϕ , and reduced Compton wavelength $\lambda_c = \hbar/(m_\phi c)$ [9, 24].

For heavy elements like Yb, the first term in Eq. 1 associated with the change in nuclear size $\delta \langle r^2 \rangle$ ('field shift' FS) dominates, while the second term is due to the electron's reduced mass and momentum correlations between electrons ('mass shift'). According to our electronic-structure calculations (see below), the third (QFS) term associated with the square of nuclear size $[\delta \langle r^2 \rangle_{ji}^2]$ represents the leading-order nonlinearity [23, 24] within the SM for Yb. The last term describes the isotope shift due

TABLE I. Inverse-mass differences μ_{ji} and measured isotope shifts ν_{ji} between next-neighboring pairs of five even Yb⁺ isotopes. μ_{ji} is calculated from the mass of Yb⁺ ions with the ionization energy set to 6.254 eV [30–32]. The nuclear size difference $\delta\langle r^2 \rangle$ is deduced from ν_{ji} using the calculated parameters $F_\alpha^{\text{CI}} = -15.852 \text{ GHz/fm}^2$, $F_\beta^{\text{CI}} = -16.094 \text{ GHz/fm}^2$, $F_\alpha^{\text{MBPT}} = -16.570 \text{ GHz/fm}^2$, $F_\beta^{\text{MBPT}} = -16.771 \text{ GHz/fm}^2$, $K_\alpha^{\text{CI}} = -1678.3 \text{ GHz} \cdot \text{u}$, and $K_\beta^{\text{CI}} = -1638.5 \text{ GHz} \cdot \text{u}$ (see SMat [33]). The uncertainties given here and throughout the paper for $\nu_{\alpha ji}$ and $\nu_{\beta ji}$ indicate 1σ statistical uncertainties; the estimated systematic uncertainties on these quantities are < 20% of the statistical uncertainties (see SMat [33]). The (170,174) pair is directly measured as a cross-check (the measurements (170,174) and (170,172), (172,174) agree within 2σ), and to improve precision (see SMat [33]). In the calculations of $\delta\langle r^2 \rangle_{ji}$ from the measured isotope shifts, the average of the values for α and β is given (the difference between transitions is less than 0.2%, see SMat [33]), and the values of K_α and K_β from the CI calculations are used for both CI and MBPT. For the data from Ref. [34] (last column), only the statistical errors are presented in the parentheses, while the systematic errors from the calculation of the electronic factors are much larger.

Isotope pair (j, i)	$\mu_{ji} [10^{-6} \text{u}^{-1}]$	$\nu_{\alpha ji} [\text{kHz}]$ $\alpha : {}^2S_{1/2} \rightarrow {}^2D_{5/2}$	$\nu_{\beta ji} [\text{kHz}]$ $\beta : {}^2S_{1/2} \rightarrow {}^2D_{3/2}$	CI	$\delta\langle r^2 \rangle_{ji} [\text{fm}^2]$ MBPT	Ref. [34]
(168, 170)	70.113 698(46)	2 179 098.93(21)	2 212 391.85(37)	-0.156	-0.149	-0.1561(3)
(170, 172)	68.506 890 50(63)	2 044 854.78(34)	2 076 421.58(39)	-0.146	-0.140	-0.1479(1)
(172, 174)	66.958 651 95(64)	1 583 068.42(36)	1 609 181.47(22)	-0.115	-0.110	-0.1207(1)
(174, 176)	65.474 078 21(65)	1 509 055.29(28)	1 534 144.06(24)	-0.110	-0.105	-0.1159(1)
(170, 174)		3 627 922.95(50)	3 685 601.95(33)			

to the Yukawa-like potential associated with the new boson ϕ . The quantities F, K, G, D are determined by the electronic wavefunctions of the transition [9, 10, 24], see SMat [33]. Note that the effect of the next-leading order Seltzer moment [24, 37] associated with $\delta\langle r^4 \rangle$ is absorbed into the QFS term, see SMat [33].

The first two terms in Eq. 1 lead to a linear relationship between the isotope shifts (King plot [15]) when one considers two different transitions α, β :

$$\bar{\nu}_{\beta ji} = K_{\beta\alpha} + F_{\beta\alpha} \bar{\nu}_{\alpha ji} + G_{\beta\alpha} \overline{[\delta\langle r^2 \rangle^2]}_{ji} + v_{ne} D_{\beta\alpha} \bar{a}_{ji} \quad (2)$$

Here we define $F_{\beta\alpha} \equiv F_\beta/F_\alpha$, $P_{\beta\alpha} \equiv P_\beta - F_{\beta\alpha} P_\alpha$ for $P \in \{K, G, D\}$, while $\bar{z}_{ji} \equiv z_{ji}/\mu_{ji}$ for $z \in \{\nu_\alpha, \nu_\beta, [\delta\langle r^2 \rangle^2], a\}$, is the inverse-mass-normalized quantity. For our purposes, where the FS dominates, the influence of mass and frequency errors is more transparent if we instead write a modified linear relationship for the frequency-normalized quantities $\bar{x}_{ji} \equiv x_{ji}/\nu_{\alpha ji}$ for $x \in \{\nu_\beta, \mu, [\delta\langle r^2 \rangle^2], a\}$

$$\bar{\nu}_{\beta ji} = F_{\beta\alpha} + K_{\beta\alpha} \bar{\mu}_{ji} + G_{\beta\alpha} \overline{[\delta\langle r^2 \rangle^2]}_{ji} + v_{ne} D_{\beta\alpha} \bar{a}_{ji} \quad (3)$$

To analyze the experimental results in this work, the transitions and isotopes are assigned as follows: $\alpha = {}^2S_{1/2} \rightarrow {}^2D_{5/2}$ (411 nm), $\beta = {}^2S_{1/2} \rightarrow {}^2D_{3/2}$ (436 nm), $j \in \{168, 170, 172, 174\}$ with $i = j + 2$, and $l = 172$.

The inset in Fig. 2a confirms the general linear relationship for the mass-normalized isotope shifts in a standard King plot corresponding to Eq. 2 for the two transitions α and β . However, when we zoom in by a factor of 10^6 (main figure 2a), we observe a small deviation from linearity, in the range 0.5 – 1 kHz in frequency units for a given data point. The frequency-normalized King plot associated with Eq. 3, as displayed in Fig. 2b, illustrates that due to the smallness of the slope, i.e. the mass shift $K_{\beta\alpha}$, the mass error along the horizontal axis $\bar{\mu}_{ji}$ has a

negligible effect. For all points taken together, the nonlinearity is non-zero at the level of 3σ (see SMat [33]).

With four independent isotope pairs, we can quantify not only the magnitude of the nonlinearity, but also an associated pattern further characterizing the nonlinearity. To this end, we introduce two dimensionless nonlinearity measures

$$\zeta_{\pm} \equiv d_{168} - d_{170} \pm (d_{172} - d_{174}) \quad (4)$$

where $d_j \equiv \bar{\nu}_{\beta ji} - f(\bar{\mu}_{ji})$ with $i = j + 2$ are the vertical deviations of the four data points $\bar{\nu}_{\beta ji}$ in Fig. 2b from the linear fit f . ζ_+ and ζ_- characterize the two possible nonlinearities for four data points, a zigzag shape with deviation pattern $+-+-$, and a curved nonlinearity with deviation pattern $+-+-$, respectively. Any given nonlinearity can be represented by a point in the $\zeta_+ \zeta_-$ plane (see Fig. 3a). A nonlinearity that arises from the coupling of the ϕ boson to the neutron number corresponds to a fixed nonlinearity pattern, and hence a given line through the origin (see SMat [33]). The same argument holds for the QFS. Our observed nonlinearity lies close to both lines representing pure coupling to a new boson and the QFS, respectively. The experimental uncertainty region in Fig. 3a can be decomposed into its possible QFS and new-boson components, as shown in Fig. 3b. It highlights the relative contributions of the two sources of nonlinearity, ranging from pure new-boson to pure QFS contribution at the current level of uncertainty. With increased measurement precision, it will be possible to separate the two contributions.

In order to convert the observed nonlinearity, as represented by ζ_{\pm} , into a physical quantity such as the coupling v_{ne} , we need to determine the associated electronic wavefunctions. To cross-check our numerical simulations for systematic errors, we use two different methods, the Dirac-Hartree-Fock method [38, 39] followed by

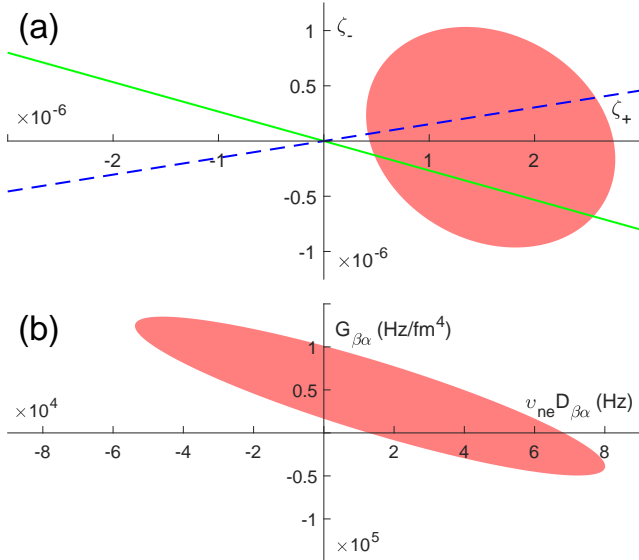


FIG. 3. (a) Nonlinearity measure (ζ_+, ζ_-) for next-neighbor isotope pairs. The red shaded region indicates the 95% confidence interval from our data. The green solid line and the blue dashed lines indicate the required ratio ζ_-/ζ_+ if the nonlinearity is purely due to a new boson ϕ and the QFS, respectively. (b) Experimental nonlinearity measure along the axes of a new boson (x -axis) and the QFS (y -axis).

the configuration interaction (CI) method [40–43], using the software package GRASP2018 [44], and many-body perturbation theory (MBPT) [45] implemented in AMBiT [46]. We calculate $F_{\beta\alpha}^{\text{CI}} = 1.0153$ and $F_{\beta\alpha}^{\text{MBPT}} = 1.0121$, within 0.2% and 0.07% of our experimental value $F_{\beta\alpha}^{\text{exp}} = 1.01141024(86)$, respectively. For the mass shift, that is more difficult to calculate accurately, we find $K_{\beta\alpha}^{\text{CI}} = 65 \text{ GHz} \cdot \text{u}$ (see SMat [33]), within a factor of 2 from the experimental value $K_{\beta\alpha}^{\text{exp}} = 120.208(23) \text{ GHz} \cdot \text{u}$. The calculated wavefunctions in combination with the measured frequency shift can also be used to extract the nuclear size difference $\delta\langle r^2 \rangle$ (see SMat [33]), in good agreement with other results [34], see Table I. We also calculate $G_{\beta\alpha}^{\text{CI}} = 232 \text{ kHz/fm}^4$ and $G_{\beta\alpha}^{\text{MBPT}} = -72 \text{ kHz/fm}^4$ for the QFS, indicating a large systematic uncertainty in the calculation of this small term. The experimentally constrained range in Fig. 3b (24 kHz/fm⁴ to 94 kHz/fm⁴, see SMat [33]) lies between the two calculated values.

Using the electronic-structure calculations, we can determine a boundary on the new-boson coupling from our data. Fig. 4 shows the upper bound on the product of couplings $|y_e y_n|$. It is obtained by dividing the experimental value of $v_{ne} D_{\beta\alpha}$ from Fig. 3b (determined with the assumption that the effect of the new boson dominates the nonlinearity; i.e., $G_{\beta\alpha} = 0$), by $(-1)^{s+1} D_{\beta\alpha}(m_\phi)/(4\pi\hbar c)$ from the atomic-structure calculations (see SMat [33] for the calculation of $D_{\beta\alpha}$). The calculations with the CI and the MBPT methods agree

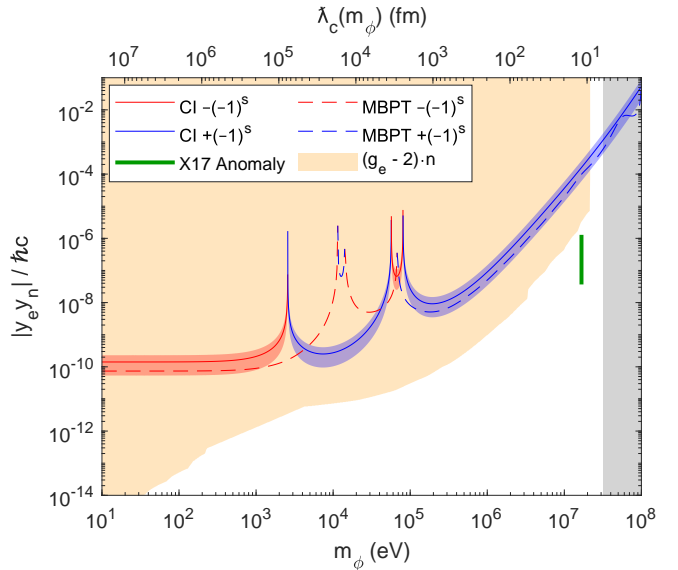


FIG. 4. Product of couplings $|y_e y_n|$ of a new boson vs. boson mass m_ϕ (bottom) and reduced Compton wavelength (top), plotted under the assumption that the observed nonlinearity in Fig. 3 is dominated by the new boson. The solid line is for the CI calculation, and the dashed line for the MBPT calculation. If the nonlinearity has a contribution from the QFS, then $|y_e y_n|$ lies below this line. The grey shade indicates the region inside the nucleus. The sign of $y_e y_n$ is color-coded: red for $-(-1)^s$ and blue for $+(-1)^s$ for a spin- s boson. The 95% confidence intervals from the statistical uncertainty in the measured isotope shift are shown as shaded areas along the solid line. The systematic uncertainty due to the wavefunction calculation is much larger, especially in the high-mass region. The thick green line indicates the preferred coupling range for the X17 boson from the Be/He anomaly [16–21]. The yellow shaded area shows the constraint from electron $g_e - 2$ measurements [47–51] combined with neutron scattering measurements [52–55] (from Ref. [10]).

with each other to better than a factor of 2 over most of the mass range m_ϕ . The upper bound from our data on $|y_e y_n|$ is ~ 200 times larger than the preferred coupling range for the X17 boson [19, 20], and two orders of magnitude larger than the bound estimated in Ref. [10] from the combination of $g - 2$ measurements on the electron and neutron scattering data. We note, however, that the limit on $|y_e|$ depends on additional assumptions about the new boson's spin and the symmetries of the interaction.

Finally, since the absolute optical frequency of the $^2S_{1/2} \rightarrow ^2D_{5/2}$ transition for $^{172}\text{Yb}^+$ has recently been measured with precision at the Hz level [56], the absolute frequencies for all the other bosonic isotopes can be deduced from our isotope shift measurements. The results are summarized in Table II.

In the future, the measurement precision can be increased by several orders of magnitude by co-trapping two isotopes [12, 13]. This improvement, also in com-

TABLE II. Frequencies of the $^2S_{1/2} \rightarrow ^2D_{5/2}$ transition.

Isotope	Absolute frequency [kHz]	Ref.
168	729 481 090 980.86(36)	this work
170	729 478 911 881.93(30)	this work
172	729 476 867 027.2068(44)	[56]
174	729 475 283 958.85(31)	this work
176	729 473 774 903.56(42)	this work

bination with measurements on additional transitions, such as the $^2S_{1/2} \rightarrow ^2F_{7/2}$ octupole transition in Yb⁺ [57] or clock transitions in neutral Yb [28, 29], will allow one to discriminate between nonlinearities of different origin. Characterizing the nonlinearities arising from within the SM can provide new information about the nucleus [58], especially in combination with improved electronic-structure calculations. On the other hand, if evidence for a new boson should emerge from the improved measurements, it can be independently verified by performing similar measurements on other atomic species [10], such as Ca/Ca⁺ [13, 59], Sr/Sr⁺ [12, 14], Nd⁺ [60], or on highly charged ions [61–64], as well as molecules like Sr₂ [65]. Unstable isotopes (e.g. ¹⁶⁶Yb with a half-life of ~ 2.4 days) can be used to increase the number of points in the King Plot, providing strong further constraints on the origin of the nonlinearity. The generalization of nonlinearity measures ζ_{\pm} for more isotopes or transitions is discussed in SMat [33].

This work was supported by the NSF and NSF CUA. This project has received funding from the European Union’s Horizon 2020 research and innovation programme under the Marie Skłodowska-Curie grant agreement No 795121. JCB is supported by the Australian Research Council (DP190100974). AK acknowledges the partial support of a William M. and Jane D. Fairbank Postdoctoral Fellowship of Stanford University. We thank M. Drewsen, V. V. Flambaum, P. Harris, N. Huntemann, T. Mehlstäubler, R. Milner, R. Ozeri, E. Peik, G. Perez, R.F. Garcia Ruiz, Y. Soreq, J. Thaler, and T. Zelevinsky for interesting discussions, W. Nazarewicz and P. Reinhard for providing information about the Yb nucleus, and V. Dzuba for pointing out the nuclear quadrupole deformation as a potential significant source of nonlinearity [26].

<https://doi.org/10.1088/0034-4885/2018/065081>.

- [3] R. Massey, T. Kitching, and J. Richard, Reports on Progress in Physics **73**, 086901 (2010), URL <https://doi.org/10.1088/0034-4885/2018/065081>.
- [4] Y. Akrami et al. (Planck Collaboration) (2018), arXiv:1807.06205, URL <https://arxiv.org/abs/1807.06205>.
- [5] M. Tanabashi et al. (Particle Data Group), Phys. Rev. D **98**, 030001 (2018), URL <https://link.aps.org/doi/10.1103/PhysRevD.98.030001>.
- [6] P. W. Graham, I. G. Irastorza, S. K. Lamoreaux, A. Lindner, and K. A. van Bibber, Annual Review of Nuclear and Particle Science **65**, 485 (2015), <https://doi.org/10.1146/annurev-nucl-102014-022120>, URL <https://doi.org/10.1146/annurev-nucl-102014-022120>.
- [7] T. E. Chupp, P. Fierlinger, M. J. Ramsey-Musolf, and J. T. Singh, Rev. Mod. Phys. **91**, 015001 (2019), URL <https://link.aps.org/doi/10.1103/RevModPhys.91.015001>.
- [8] M. S. Safronova, D. Budker, D. DeMille, D. F. J. Kimball, A. Derevianko, and C. W. Clark, Rev. Mod. Phys. **90**, 025008 (2018), URL <https://link.aps.org/doi/10.1103/RevModPhys.90.025008>.
- [9] C. Delaunay, R. Ozeri, G. Perez, and Y. Soreq, Phys. Rev. D **96**, 093001 (2017), URL <https://link.aps.org/doi/10.1103/PhysRevD.96.093001>.
- [10] J. C. Berengut, D. Budker, C. Delaunay, V. V. Flambaum, C. Frugueule, E. Fuchs, C. Grojean, R. Harnik, R. Ozeri, G. Perez, et al., Phys. Rev. Lett. **120**, 091801 (2018), URL <https://link.aps.org/doi/10.1103/PhysRevLett.120.091801>.
- [11] F. Gebert, Y. Wan, F. Wolf, C. N. Angstmann, J. C. Berengut, and P. O. Schmidt, Phys. Rev. Lett. **115**, 053003 (2015), URL <https://link.aps.org/doi/10.1103/PhysRevLett.115.053003>.
- [12] T. Manovitz, R. Shaniv, Y. Shapira, R. Ozeri, and N. Akerman, Phys. Rev. Lett. **123**, 203001 (2019), URL <https://link.aps.org/doi/10.1103/PhysRevLett.123.203001>.
- [13] F. W. Knollmann, A. N. Patel, and S. C. Doret, Phys. Rev. A **100**, 022514 (2019), URL <https://link.aps.org/doi/10.1103/PhysRevA.100.022514>.
- [14] H. Miyake, N. C. Pisenti, P. K. Elgee, A. Sitaram, and G. K. Campbell, Phys. Rev. Research **1**, 033113 (2019), URL <https://link.aps.org/doi/10.1103/PhysRevResearch.1.033113>.
- [15] W. H. King, *Isotope Shifts in Atomic Spectra* (Plenum Press, 1984).
- [16] A. J. Krasznahorkay, M. Csatlós, L. Csige, Z. Gácsi, J. Gulyás, Á. Nagy, N. Sas, J. Timár, T. G. Tornyai, I. Vajda, et al., Journal of Physics: Conference Series **1056**, 012028 (2018), ISSN 1742-6596, URL <https://stacks.iop.org/1742-6596/1056/i=1/a=012028?key=crossref.10a8b6db295a5c09f5d12be531be382e>.
- [17] A. J. Krasznahorkay, M. Csatlós, L. Csige, Z. Gácsi, J. Gulyás, M. Hunyadi, I. Kuti, B. M. Nyakó, L. Stuhl, J. Timár, et al., Phys. Rev. Lett. **116**, 042501 (2016), URL <https://link.aps.org/doi/10.1103/PhysRevLett.116.042501>.
- [18] A. J. Krasznahorkay, M. Csatlós, L. Csige, J. Gulyás, M. Koszta, B. Szihalmi, J. Timar, D. S. Firak, A. Nagy, N. J. Sas, et al. (2019), 1910.10459.

* These authors contributed equally to this work.

[†] vuletic@mit.edu

- [1] V. C. Rubin, W. K. Ford, and N. Thonnard, Astrophys. J. **238**, 471 (1980), URL <http://adsbit.harvard.edu/full/1980ApJ...238..471R/0000471.000.html>.
- [2] D. Clowe, M. Bradač, A. H. Gonzalez, M. Markevitch, S. W. Randall, C. Jones, and D. Zaritsky, The Astrophysical Journal **648**, L109 (2006), URL <https://doi.org/10.1086/508162>.

[19] J. L. Feng, B. Fornal, I. Galon, S. Gardner, J. Smolinsky, T. M. P. Tait, and P. Tanedo, *Phys. Rev. Lett.* **117**, 071803 (2016), URL <https://link.aps.org/doi/10.1103/PhysRevLett.117.071803>.

[20] J. L. Feng, B. Fornal, I. Galon, S. Gardner, J. Smolinsky, T. M. P. Tait, and P. Tanedo, *Phys. Rev. D* **95**, 035017 (2017), URL <https://link.aps.org/doi/10.1103/PhysRevD.95.035017>.

[21] U. D. Jentschura and I. N  ndori, *Phys. Rev. A* **97**, 042502 (2018), URL <https://link.aps.org/doi/10.1103/PhysRevA.97.042502>.

[22] D. Banerjee, V. E. Burtsev, A. G. Chumakov, D. Cooke, P. Crivelli, E. Depero, A. V. Dermenev, S. V. Donskov, R. R. Dusaev, T. Enik, et al. (NA64 Collaboration), *Phys. Rev. Lett.* **120**, 231802 (2018), URL <https://link.aps.org/doi/10.1103/PhysRevLett.120.231802>.

[23] V. V. Flambaum, A. J. Geddes, and A. V. Viatkina, *Phys. Rev. A* **97**, 032510 (2018), URL <https://link.aps.org/doi/10.1103/PhysRevA.97.032510>.

[24] K. Mikami, M. Tanaka, and Y. Yamamoto, *The European Physical Journal C* **77**, 896 (2017), ISSN 1434-6052, URL <https://doi.org/10.1140/epjc/s10052-017-5467-4>.

[25] M. Tanaka and Y. Yamamoto (2019), 1911.05345.

[26] S. O. Allehabi, V. A. Dzuba, V. V. Flambaum, A. V. Afanasjev, and S. E. Agbemava (2020), 2001.09422.

[27] N. Huntemann, C. Sanner, B. Lipphardt, C. Tamm, and E. Peik, *Phys. Rev. Lett.* **116**, 063001 (2016), URL <https://link.aps.org/doi/10.1103/PhysRevLett.116.063001>.

[28] Z. W. Barber, C. W. Hoyt, C. W. Oates, L. Hollberg, A. V. Taichenachev, and V. I. Yudin, *Phys. Rev. Lett.* **96**, 083002 (2006), URL <https://link.aps.org/doi/10.1103/PhysRevLett.96.083002>.

[29] M. S. Safranova, S. G. Porsev, C. Sanner, and J. Ye, *Phys. Rev. Lett.* **120**, 173001 (2018), URL <https://link.aps.org/doi/10.1103/PhysRevLett.120.173001>.

[30] W. Huang, G. Audi, M. Wang, F. G. Kondev, S. Naimi, and X. Xu, *Chinese Physics C* **41**, 030002 (2017), URL <https://doi.org/10.1088%2F1674-1137%2F41%2F3%2F030002>.

[31] M. Wang, G. Audi, F. G. Kondev, W. Huang, S. Naimi, and X. Xu, *Chinese Physics C* **41**, 030003 (2017), URL <https://doi.org/10.1088%2F1674-1137%2F41%2F3%2F030003>.

[32] R. Rana, M. H  cker, and E. G. Myers, *Phys. Rev. A* **86**, 050502 (2012), URL <https://link.aps.org/doi/10.1103/PhysRevA.86.050502>.

[33] See supplemental material at xxx link.

[34] I. Angeli and K. Marinova, *Atomic Data and Nuclear Data Tables* **99**, 69 (2013), ISSN 0092-640X, URL <http://www.sciencedirect.com/science/article/pii/S0092640X12000265>.

[35] M. Cetina, A. Bylinskii, L. Karpa, D. Gangloff, K. M. Beck, Y. Ge, M. Scholz, A. T. Grier, I. Chuang, and V. Vuleti  , *New Journal of Physics* **15**, 053001 (2013), URL <https://doi.org/10.1088%2F1367-2630%2F15%2F5%2F053001>.

[36] P. Taylor, M. Roberts, S. V. Gateva-Kostova, R. B. M. Clarke, G. P. Barwood, W. R. C. Rowley, and P. Gill, *Phys. Rev. A* **56**, 2699 (1997), URL <https://link.aps.org/doi/10.1103/PhysRevA.56.2699>.

[37] E. C. Seltzer, *Phys. Rev.* **188**, 1916 (1969), URL <https://link.aps.org/doi/10.1103/PhysRev.188.1916>.

[38] I. Grant, B. McKenzie, P. Norrington, D. Mayers, and N. Pyper, *Computer Physics Communications* **21**, 207 (1980), ISSN 0010-4655, URL <http://www.sciencedirect.com/science/article/pii/0010465580900417>.

[39] K. Dyall, I. Grant, C. Johnson, F. Parpia, and E. Plummer, *Computer Physics Communications* **55**, 425 (1989), ISSN 0010-4655, URL <http://www.sciencedirect.com/science/article/pii/0010465589901367>.

[40] P. J  nsson, A. Ynnerman, C. Froese Fischer, M. R. Godefroid, and J. Olsen, *Phys. Rev. A* **53**, 4021 (1996), URL <https://link.aps.org/doi/10.1103/PhysRevA.53.4021>.

[41] S. G. Porsev, M. G. Kozlov, and D. Reimers, *Phys. Rev. A* **79**, 032519 (2009), URL <https://link.aps.org/doi/10.1103/PhysRevA.79.032519>.

[42] B. Fawcett and M. Wilson, *Atomic Data and Nuclear Data Tables* **47**, 241 (1991), ISSN 0092-640X, URL <http://www.sciencedirect.com/science/article/pii/0092640X9190003M>.

[43] E. Bi  mont, J.-F. Dutrieux, I. Martin, and P. Quinet, *Journal of Physics B: Atomic, Molecular and Optical Physics* **31**, 3321 (1998), URL <https://doi.org/10.1088%2F0953-4075%2F31%2F15%2F006>.

[44] C. Froese Fischer, G. Gaigalas, P. J  nsson, and J. Biero  , *Computer Physics Communications* **237**, 184 (2019), ISSN 0010-4655, URL <http://www.sciencedirect.com/science/article/pii/S0010465518303928>.

[45] V. A. Dzuba, V. V. Flambaum, P. G. Silvestrov, and O. P. Sushkov, *Journal of Physics B: Atomic and Molecular Physics* **18**, 597 (1985), URL <https://doi.org/10.1088%2F0022-3700%2F18%2F4%2F008>.

[46] E. Kahl and J. Berengut, *Computer Physics Communications* **238**, 232 (2019), ISSN 0010-4655, URL <http://www.sciencedirect.com/science/article/pii/S0010465518304302>.

[47] D. Hanneke, S. Fogwell, and G. Gabrielse, *Phys. Rev. Lett.* **100**, 120801 (2008), URL <https://link.aps.org/doi/10.1103/PhysRevLett.100.120801>.

[48] D. Hanneke, S. Fogwell Hoogerheide, and G. Gabrielse, *Phys. Rev. A* **83**, 052122 (2011), URL <https://link.aps.org/doi/10.1103/PhysRevA.83.052122>.

[49] T. Aoyama, M. Hayakawa, T. Kinoshita, and M. Nio, *Phys. Rev. Lett.* **109**, 111807 (2012), URL <https://link.aps.org/doi/10.1103/PhysRevLett.109.111807>.

[50] R. Bouchendira, P. Clad  , S. Guellati-Kh  lifa, F. Nez, and F. Biraben, *Phys. Rev. Lett.* **106**, 080801 (2011), URL <https://link.aps.org/doi/10.1103/PhysRevLett.106.080801>.

[51] H. Davoudiasl, H.-S. Lee, and W. J. Marciano, *Phys. Rev. D* **89**, 095006 (2014), URL <https://link.aps.org/doi/10.1103/PhysRevD.89.095006>.

[52] R. Barbieri and T. Ericson, *Physics Letters B* **57**, 270 (1975), ISSN 0370-2693, URL <http://www.sciencedirect.com/science/article/pii/0370269375900738>.

[53] H. Leeb and J. Schmiedmayer, *Phys. Rev. Lett.* **68**, 1472 (1992), URL <https://link.aps.org/doi/10.1103/PhysRevLett.68.1472>.

[54] Y. N. Pokotilovski, *Physics of Atomic Nuclei* **69**, 924 (2006), URL <https://doi.org/10.1134/S1063778806060020>.

[55] V. V. Nesvizhevsky, G. Pignol, and K. V. Protasov, *Phys. Rev. D* **77**, 034020 (2008), URL <https://link.aps.org/doi/10.1103/PhysRevD.77.034020>.

doi/10.1103/PhysRevD.77.034020.

[56] H. A. Fürst, C.-H. Yeh, D. Kalincev, A. P. Kulosa, L. S. Dreissen, R. Lange, E. Benkler, N. Huntemann, E. Peik, and T. E. Mehlstäubler (2020), 2006.14356.

[57] M. Roberts, P. Taylor, G. P. Barwood, P. Gill, H. A. Klein, and W. R. C. Rowley, Phys. Rev. Lett. **78**, 1876 (1997), URL <https://link.aps.org/doi/10.1103/PhysRevLett.78.1876>.

[58] P.-G. Reinhard, W. Nazarewicz, and R. F. Garcia Ruiz, Phys. Rev. C **101**, 021301 (2020), URL <https://link.aps.org/doi/10.1103/PhysRevC.101.021301>.

[59] A. Mortensen, J. J. T. Lindballe, I. S. Jensen, P. Staanum, D. Voigt, and M. Drewsen, Phys. Rev. A **69**, 042502 (2004), URL <https://link.aps.org/doi/10.1103/PhysRevA.69.042502>.

[60] N. Bhatt, K. Kato, and A. C. Vutha (2020), 2002.08290.

[61] P. Micke, T. Leopold, S. A. King, E. Benkler, L. J. Spieß, L. Schmöger, M. Schwarz, J. R. Crespo López-Urrutia, and P. O. Schmidt, Nature **578**, 60 (2020), ISSN 0028-0836, URL <http://dx.doi.org/10.1038/s41586-020-1959-8> <http://www.nature.com/articles/s41586-020-1959-8>.

[62] V. A. Yerokhin, R. A. Müller, A. Surzhykov, P. Micke, and P. O. Schmidt, Phys. Rev. A **101**, 012502 (2020), URL <https://link.aps.org/doi/10.1103/PhysRevA.101.012502>.

[63] R. Silwal, A. Lapierre, J. D. Gillaspy, J. M. Dreiling, S. A. Blundell, Dipti, A. Borovik, G. Gwinner, A. C. C. Villari, Y. Ralchenko, et al., Phys. Rev. A **98**, 052502 (2018), URL <https://link.aps.org/doi/10.1103/PhysRevA.98.052502>.

[64] M. G. Kozlov, M. S. Safronova, J. R. Crespo López-Urrutia, and P. O. Schmidt, Rev. Mod. Phys. **90**, 045005 (2018), URL <https://link.aps.org/doi/10.1103/RevModPhys.90.045005>.

[65] B. H. McGuyer, M. McDonald, G. Z. Iwata, M. G. Tarallo, A. T. Grier, F. Apfelbeck, and T. Zelevinsky, New Journal of Physics **17**, 055004 (2015), URL <https://doi.org/10.1088%2F1367-2630%2F17%2F5%2F055004>.

Supplementary Material: 3σ Nonlinear Isotope Shift in Yb^+ Search for New Boson

Ian Counts,^{1,*} Joonseok Hur,^{1,*} Diana P. L. Aude Craik,¹ Honggi Jeon,² Calvin Leung,¹ Julian C. Berengut,³ Amy Geddes,³ Akio Kawasaki,⁴ Wonho Jhe,² and Vladan Vuletić^{1,†}

¹*Department of Physics and Research Laboratory of Electronics,*

Massachusetts Institute of Technology, Cambridge, Massachusetts 02139, USA

²*Department of Physics and Astronomy, Seoul National University, Seoul 151-747, Korea*

³*School of Physics, University of New South Wales, Sydney, New South Wales 2052, Australia*

⁴*W. W. Hansen Experimental Physics Laboratory and Department of Physics,*

Stanford University, Stanford, California 94305, USA

I. EXPERIMENTAL DETAILS

We trap a single Yb^+ ion $135\ \mu\text{m}$ above the surface of a lithographic microchip, described in detail in Ref. [1]. The ion is Doppler-cooled on the $6s\ ^2S_{1/2} \rightarrow 6p\ ^2P_{1/2}$ transition by a 369-nm laser beam aligned parallel to the chip surface, and at a diagonal to the trap axis. This beam has a component along all motional modes of the trapped ion, and hence cools all motional degrees of freedom simultaneously. The ion occasionally decays to the $5d\ ^2D_{3/2}$ state from $^2P_{1/2}$ during the cooling cycle (branching ratio = 0.5% [2]; occurs once every $\sim 150\ \mu\text{s}$ in our system), and is subsequently returned to the cooling cycle via a repumper at 935 nm. Once every few minutes, the ion can also decay to the $4f^{13}6s^2\ ^2F_{7/2}$ state, and must be repumped at 638 nm. The cooling laser and both repumpers have isotope shifts of a few GHz [3–5].

To drive the probe transitions at 411 nm ($6s\ ^2S_{1/2} \rightarrow 5d\ ^2D_{5/2}; \Gamma/(2\pi) = 22\ \text{Hz}$ [6]) and 436 nm ($6s\ ^2S_{1/2} \rightarrow 5d\ ^2D_{3/2}; \Gamma/(2\pi) = 3\ \text{Hz}$ [7]), we employ a Ti:Sapphire probe laser, tuned to 822 nm and 871 nm, respectively. This laser is frequency-stabilized via the Pound-Drever-Hall (PDH) protocol to an ultra-low-expansion-spaced (ULE-spaced) cavity that has finesse $\mathcal{F} \sim 50000$ and linewidth $\kappa/(2\pi) = 30\ \text{kHz}$. By frequency-stabilizing a sideband produced by an electro-optic modulator (EOM) to the cavity, a coarse spectroscopic frequency scan can be engineered via tuning the sideband frequency. The infrared light is fiber-coupled to one of two potassium titanyl phosphate (KTP) waveguide doublers, which output 411 nm and 436 nm light, respectively. The blue light, of linewidth $\sim 1\ \text{kHz}$, is then passed through an acousto-optic modulator (AOM), which can be used for finer frequency tuning, and focused down through an achromatic lens to a beam waist of radius $w_0 = 15\ \mu\text{m}$ at the trapped ion. In order to align the probe beam to the ion, 369-nm light is overlapped with the probe. The 369-nm and the probe beams are focused through the same achromatic lens, and alignment is verified by the resulting fluorescence re-radiated off the ion. The powers of

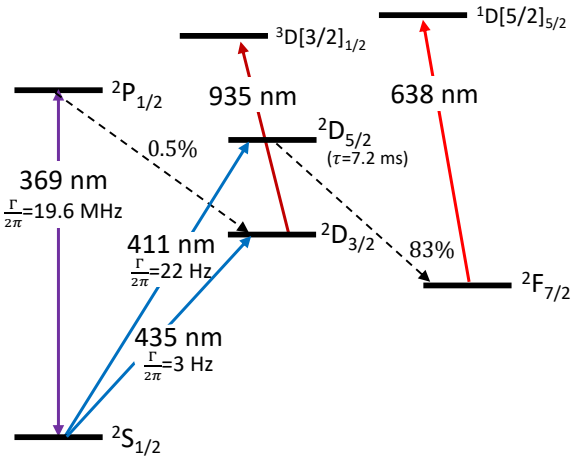


FIG. S1. Partial Yb^+ level diagram.

the 411 and 436 nm beams at the location of the ion are $1.1\ \text{mW}$ and $0.2\ \text{mW}$, respectively. The relevant levels, lasers (cooling, probe, and repumper lasers), and decays are illustrated in Fig. S1.

The readout of the state is carried out via an *electron-shelving scheme* [6]. In order to probe the ion in the dark and avoid AC Stark shifts, the 369 nm cooling light and the probe light (411 nm or 436 nm) are alternatively applied. Ions in the ground state $S_{1/2}$ are detected via fluorescence during the cooling with 369 nm light. If the ion is fluorescing before a probe pulse and no longer fluorescing afterwards, the ion is said to have completed a quantum jump. Otherwise, the ion failed to quantum jump (or, if there was no fluorescence before the probe pulse, the ion failed to be initialized). By dividing the number of quantum jumps by the total number of successful initialization, we can measure a probability of excitation as a function of frequency. The details of the pulse sequences used to implement this protocol for the 411 nm and the 436 nm transitions are described in sections I A and I B, respectively.

The precise frequency of either clock transition is determined via Ramsey spectroscopy, with $\frac{\pi}{2}$ times of $\sim 5\ \mu\text{s}$ and interrogation times of $10\ \mu\text{s}$. A small magnetic field is applied to the ion to compensate for Earth's magnetic field, and an additional magnetic field of $\sim 1.1\ \text{G}$ is

* These authors contribute equally to this work.

† vuletic@mit.edu

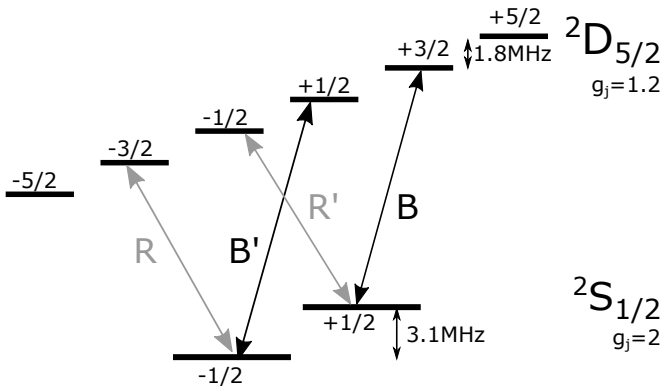


FIG. S2. The Zeeman transition pair measured to determine the 411 nm transition center is labelled R and B . Estimated Stark shifts due to off-resonant driving of transitions R' and B' are listed in table S2.

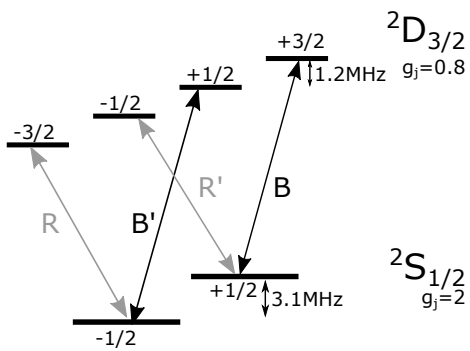


FIG. S3. The Zeeman transition pair measured to determine the 436 nm transition center is labelled R and B . Estimated Stark shifts due to off-resonant driving of transitions R' and B' are listed in table S2.

applied along the probe beam to separate different Zeeman components of the transition. The probe laser frequency is scanned (in steps of 2–4 kHz) over the central Ramsey fringe of a pair of transitions, symmetrically detuned from the center frequency, between Zeeman components of the ground and excited states. This pair of transitions, labelled B and R as indicated in Figs. S2 and Fig. S3, is identified via a wide scan with a single pulse of the probe beam applied in each measurement cycle (see Fig. S4, for instance). Fig. S5 shows an example Ramsey spectrum of one Zeeman component of the 436 nm transition. Fig. S6 shows a probe-pulse-length scan performed on the transition (Rabi flopping), which is used to determine the $\pi/2$ time to be used in the Ramsey sequence.

Five scans over each of the red-detuned and blue-detuned symmetric Zeeman transitions (transitions R and B respectively in Figs. S2, S3) are interleaved. Each set of scans is repeated two to three times for each isotope. We establish a center frequency for the probed transition by averaging the frequencies of R and B . For each measurement of B 's frequency, a pair of measure-

ments of R 's frequency taken before and after the measurement of B are used to interpolate the frequency of R at the time when B was measured. The same is done for each measurement of R (using pairs of measurements of B taken before and after the measurement of R). Measurements of transition center are then determined by averaging the frequency of the B (R) and the interpolated frequency of R (B).

To measure the isotope shift between two isotopes i and j , a single ion of isotope i is first selected and loaded by tuning the frequency of a photo-ionizing beam aligned to a stream of neutral Yb atoms emitted from an oven. Cooling and repumping beams are also tuned as required. Once isotope i is loaded, the Ramsey measurement described in the previous paragraph is repeated multiple times. The lasers are then re-tuned to load isotope j . The probe beam is tuned (but is kept locked to the same cavity free spectral range (FSR)), and the Ramsey measurements are again carried out. The measurements on i and j are then repeated, with each isotope measured between two and three times. While the absolute frequencies of the clock transitions for different isotopes are not measured independently, this method allows the measurement of a relative isotope shift with precision on the order of \sim 300 Hz (see Fig. 2 and Table I in the main text). The isotope shifts of four nearest pairs of stable even Yb isotopes (i.e., $j = 168, 170, 172, 174$ and $i = j+2$) were measured for each transition. By comparing this precision shift measurement with a previously measured absolute frequency for the $^{172}\text{Yb}^+$ isotope [8], absolute frequencies for the 411 nm transition can also be determined (Table II in the main text).

A. Measurements on the $^2\text{S}_{1/2} \rightarrow ^2\text{D}_{5/2}$ transition at $\alpha = 411$ nm

The pulse sequence applied at each point of the frequency scans used to probe the 411 nm transition is depicted schematically in Fig. S7. The sequence is comprised of three sections: initialization, probe and readout. Its total duration is 200 ms. During initialization, the ion is Doppler-cooled on the 369 nm transition. After cooling, a $40\ \mu\text{s}$ optical pumping pulse is used to initialize the ion in the $m_j = -\frac{1}{2}$ or $m_j = +\frac{1}{2}$ level of the $^2\text{S}_{1/2}$ ground state with σ^- or σ^+ -polarized 369 nm light, respectively. This is followed by the probe period, where a Ramsey sequence is applied using 411 nm light (the Ramsey interval used was $10\ \mu\text{s}$, and the $\frac{\pi}{2}$ -pulse length was $\sim 5\ \mu\text{s}$). During the Ramsey sequence, the 369 nm is extinguished by an AOM. The probe sequence is followed by a readout pulse of 369 nm light, during which the ion's time-resolved fluorescence is measured and recorded by a photomultiplier tube (PMT) synchronized to a field-programmable gate array-based (FPGA-based) data acquisition system. The sum of the fluorescence counts recorded over the first three 2 ms bins in the readout part of the sequence is then compared to the sum of the fluo-

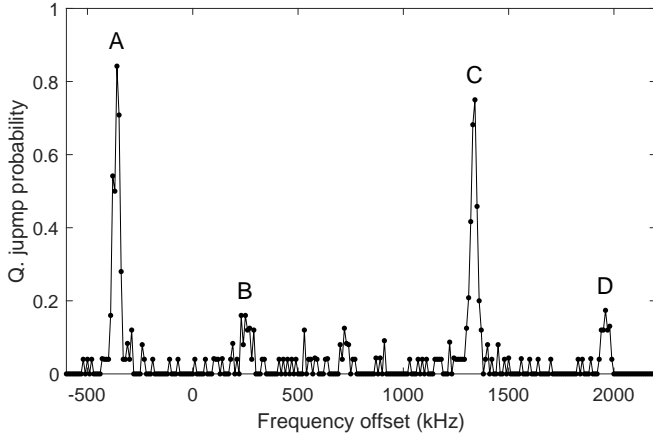


FIG. S4. A broad spectrum taken across four Zeeman components of the 411 nm transition, probed via a single pulse. The Zeeman shift agrees with calculated g-factors for the 411 nm transition and the magnetic field magnitude of 1.1 G. Note that optical pumping suppresses two of the Zeeman components and enhances their respective opposites. The components shown are:

- (A) $|S_{1/2}, m_J = 1/2\rangle \rightarrow |D_{5/2}, m_J = -1/2\rangle$,
- (B) $|S_{1/2}, m_J = -1/2\rangle \rightarrow |D_{5/2}, m_J = -3/2\rangle$,
- (C) $|S_{1/2}, m_J = 1/2\rangle \rightarrow |D_{5/2}, m_J = 3/2\rangle$,
- (D) $|S_{1/2}, m_J = -1/2\rangle \rightarrow |D_{5/2}, m_J = 1/2\rangle$.

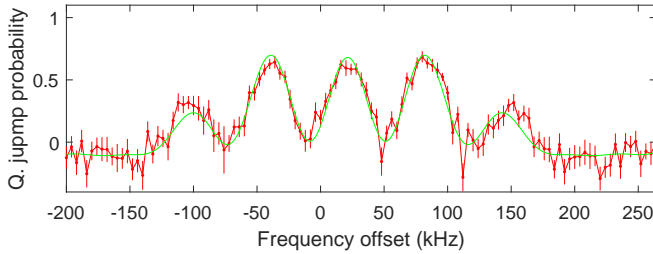


FIG. S5. Ramsey spectrum on a single Zeeman component of the 436-nm transition with fit (green solid curve). The x-axis is the frequency of the probe beam with an arbitrary offset. The quantum jump probability is obtained by taking the fractional difference between the integrated readout fluorescence and the integrated calibration fluorescence; see section IB.

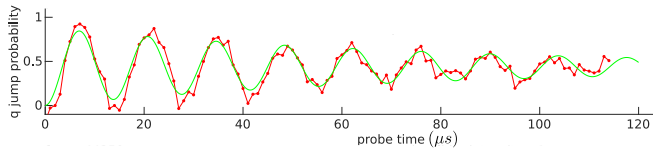


FIG. S6. Rabi oscillations for a Zeeman component of the 436-nm transition. The measured quantum jump probability is plotted against the scanned probe pulse length. The Rabi oscillation is fitted to determine the $\frac{\pi}{2}$ time, which is used in the Ramsey sequence that we apply to probe the transition. The quantum jump probability is obtained by taking the fractional difference between the integrated readout fluorescence and the integrated calibration fluorescence; see section IB.

rescence counts recorded over the last three 2 ms bins in the initialization part of the sequence. The fluorescence counts are then compared to a previously-established threshold. If above the threshold, the ion is taken to be in the ground state and is labelled as “bright”. If the initialization counts do not indicate a “bright” ion, this implies initialization has failed and there was no opportunity for a quantum jump to occur, since the ion was not in the ground state before the probe sequence. In this case, the sequence is not counted towards the total number of shots. A quantum jump is taken to have occurred if the ion is dark at readout (i.e. readout counts are equal to or below threshold) and bright at initialization. The sequence is repeated 35 times and a quantum-jump probability is established by taking the ratio of the number of quantum jumps that occurred to the number of attempts with successful initialization.

It should also be noted that the 638-nm repumper light is kept on during the initialization stage in order to repump any population that may have decayed from $^2D_{5/2}$ to $^2F_{7/2}$ (branching ratio = 83% [6]). The main cause of initialization failure is unsuccessful repumping of this population to the $^2S_{1/2}$ ground state by the 638-nm repumper, which has a repumping time constant of $\gtrsim 200$ ms.

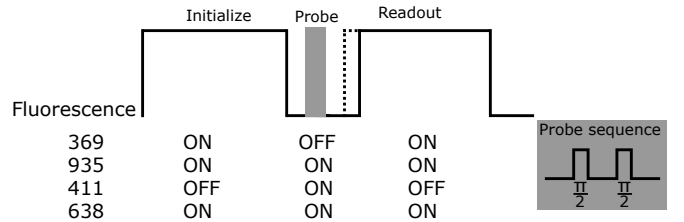


FIG. S7. Pulse sequence used to probe the 411-nm transition.

B. Measurements on the $^2S_{1/2} \rightarrow ^2D_{3/2}$ transition at $\beta = 436$ nm

The pulse sequence with single-shot readout of quantum jumps that is used for probing the 411-nm transition cannot be used when probing the 436-nm transition. This is because the upper state of the 436-nm transition can be populated not only by a probe-induced quantum jump from the $^2S_{1/2}$ ground state, but also by spontaneous decay from the $^2P_{1/2}$ excited state. Single-shot readout of the fluorescence on the 369 nm transition would not distinguish between these two scenarios.

Instead, we employ the pulse sequence depicted in Fig. S8 to probe this transition. The first half of the sequence is comprised of an initialization pulse with both the 369-nm and the 935-nm lasers applied, as before, followed by a time-resolved fluorescence readout with only the 369-nm beam. This readout serves to calibrate the effect of population decay from $^2P_{1/2}$ to the $^2D_{3/2}$ – without the 935-nm repumper, population will eventually be

pumped to the $^2D_{3/2}$ dark state. The same initialization and readout sequence is then repeated after the Ramsey probe sequence has been applied. When averaged over several applications of the sequence (we perform 2000 shots of the sequence, which corresponds to a 1s integration time for a 500- μ s-long sequence; 8-10 repeats of this 1 s integration time are then performed), this second readout will show a smaller peak height in fluorescence if the 436 nm transition is being driven. A quantum jump probability is hence obtained by taking the fractional difference between the averaged fluorescence counts integrated over all time bins of the second readout and the counts integrated over all time bins of the first calibration readout.

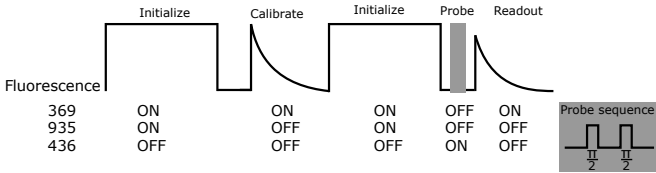


FIG. S8. Pulse sequence used to probe 436 nm transition. The solid curve indicates the time-resolved fluorescence by the ion.

II. DATA ANALYSIS

A set of measured center frequencies of a transition for a pair of isotopes over the course of ~ 10 hours are fitted with the linear model:

$$y_k = a + bt_k + cz_k \quad (S1)$$

where k indexes each data point; y_k is the measured transition frequency; t_k is the time at which point k was measured; $z_k = 1$ if the point k is for isotope j and $z_k = 0$ for reference isotope i ; and a , b , and c are fitting parameters. The first two terms account for the linear drift of the length of the reference cavity. The last term describes the isotope shift; with z_k set to 0 or 1, c represents the fitted isotope shift.

To determine the uncertainty in the measured isotope shifts, bootstrapping statistics are employed [9]. A new set of data points is formed by re-sampling points from the set of measured data points, allowing for multiple instances of the each point, until the number of elements in the re-sampled set is the same as that of the original set. The fitting described in the previous paragraph is applied to the re-sampled set to find a value for the isotope shift. Repeating the procedure N times (with sufficiently large N) gives the histogram of isotope shifts from each re-sampled set. The mean and standard deviation of the distribution are taken as the measured isotope shift and its uncertainty, respectively. Fig. S9 shows examples of the measured transition frequencies over time, the fitted linear drift of the reference FSR, and the bootstrapping

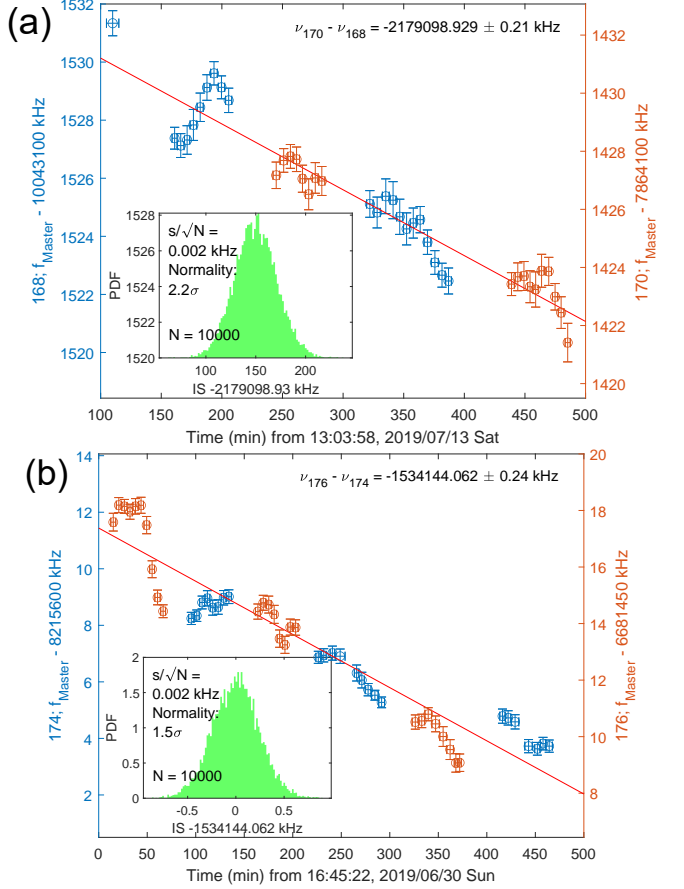


FIG. S9. Frequencies of (a) 411 nm transition in $^{168}\text{Yb}^+$ (blue; left y-axis) and $^{170}\text{Yb}^+$ (orange; right y-axis), and (b) 436 nm transition in $^{174}\text{Yb}^+$ (blue; left y-axis) and $^{176}\text{Yb}^+$ (orange; right y-axis). Transition frequencies of both isotopes over time were fitted with linear model (red line, see Eq. S1). The insets show the distribution of fitted isotope shifts from bootstrapping with $N = 10^4$ re-sampling.

statistics (see insets). Drifts in the probe laser frequency with time are visible in Fig. S9. We discuss estimates of systematic shifts in section IV.

The isotope shifts between nearest even isotopes are measured for each transition. Additionally, the isotope shift between ^{170}Yb and ^{174}Yb is measured as a cross-check. The results are listed in table I in the main text. Using the additional $(j, i) = (170, 174)$ measurement, the precision of the isotope shifts $\nu_{\alpha j i}$'s for $(170, 172)$, $(172, 174)$, and $(170, 174)$ can be improved in the standard way by adding and averaging measured values:

$$\begin{aligned} \nu'_1 &= \frac{\sigma_1'^2}{\sigma_1^2} \nu_1 + \frac{\sigma_1'^2}{\sigma_2^2 + \sigma_3^2} (\nu_3 - \nu_2) & \frac{1}{\sigma'_1'^2} &= \frac{1}{\sigma_1^2} + \frac{1}{\sigma_2^2 + \sigma_3^2} \\ \nu'_2 &= \frac{\sigma_2'^2}{\sigma_2^2} \nu_2 + \frac{\sigma_2'^2}{\sigma_3^2 + \sigma_1^2} (\nu_3 - \nu_1) & \frac{1}{\sigma'_2'^2} &= \frac{1}{\sigma_2^2} + \frac{1}{\sigma_3^2 + \sigma_1^2} \\ \nu'_3 &= \frac{\sigma_3'^2}{\sigma_3^2} \nu_3 + \frac{\sigma_3'^2}{\sigma_1^2 + \sigma_2^2} (\nu_1 + \nu_2) & \frac{1}{\sigma'_3'^2} &= \frac{1}{\sigma_3^2} + \frac{1}{\sigma_1^2 + \sigma_2^2}, \end{aligned} \quad (S2)$$

TABLE S1. Isotope shifts ν'_{ji} 's between $(j, i = j + 2) = (170, 172)$, $(172, 174)$, and $(170, 174)$ isotope pairs after the precision is improved. The values are correlated to each other for each transition.

Isotope pair (j, i)	$\nu'_{\alpha ji}$ [kHz] $\alpha : {}^2S_{1/2} \rightarrow {}^2D_{5/2}$	$\nu'_{\beta ji}$ [kHz] $\beta : {}^2S_{1/2} \rightarrow {}^2D_{3/2}$
(170, 172)	2 044 854.73(30)	2 076 421.04(28)
(172, 174)	1 583 068.35(31)	1 609 181.29(20)
(170, 174)	3 627 923.08(35)	3 685 602.34(27)

where ν_q and σ_q refer to the measured shift $\nu_{\alpha ji}$ and its uncertainty, respectively, for $q = 1$: (170, 172), $q = 2$: (172, 174), and $q = 3$: (170, 174) pairs, and ν'_q and σ'_q represent the values with the (170, 174) measurement included. The results are shown in table S1. Through this procedure, however, the isotope shifts ν'_1 , ν'_2 , and ν'_3 become correlated to each other. To take the correlation into account, the generalized-least-squares (GLS) method is used to fit the points in King plot (Fig. 2 in the main text). We extract the p -value of the χ^2_k distribution, with $k = 2$ being the degree of freedom of the fitting (for four data points and two fitting parameters). We find $\chi^2 = 11.7$ with a p -value of 0.0029, corresponding to a significance of 3σ .

There are different ways of choosing the reference isotope, and the choice determines the correlation between errors. When the latter are included carefully in the analysis, the same significance of nonlinearity, within $\pm 0.001\sigma$, is obtained for all reference choices. The confidence intervals of the nonlinearity measures, parametrized by $v_{ne}D_{\beta\alpha}$ and $G_{\beta\alpha}$ (Fig. 3b in the main text), from different reference choices also agree.

To obtain the nonlinearity pattern from the known possible sources (e.g., $G_{\alpha}[\delta(r^2)^2]_{ji}$ or $v_{ne}D_{\alpha}a_{ji}$), the four points $(\bar{\nu}_{\alpha ji}, z_{ji})$ are fitted in the same way the King plot is fitted, where z_{ji} is the nuclear factor of the source term (e.g. $[\delta(r^2)^2]_{ji}$ or a_{ji}). The residuals of the fitting show the nonlinearity pattern of the source, and the corresponding nonlinearity measure ζ_{\pm}^z is obtained via Eq. 4. The direction of the nonlinearity lines is given as the ratio ζ_{-}^z/ζ_{+}^z , as in Fig. 3a. Note that the *pattern* is determined by nuclear factors while the electronic factors only scale the overall size of residuals.

III. SUPPRESSED EFFECT OF MASS UNCERTAINTY

The uncertainties in $\bar{\nu}_{\alpha ji}$ and $\bar{\nu}_{\beta ji}$ due to the uncertainties in μ_{ji} from the measured masses are correlated as the change in μ_{ji} modifies both $\bar{\nu}_{\alpha ji}$ and $\bar{\nu}_{\beta ji}$. If the ratio of the change

$$\frac{\partial \bar{\nu}_{\beta ji}/\partial \mu_{ji}}{\partial \bar{\nu}_{\alpha ji}/\partial \mu_{ji}} = \frac{\nu_{\beta ji}}{\nu_{\alpha ji}} \quad (\text{S3})$$

is parallel to the slope of the King plot $F_{\beta\alpha}$, the effect of mass uncertainty will be suppressed. The suppression factor is given as the difference between the ratio $\nu_{\beta ji}/\nu_{\alpha ji}$ and the slope $F_{\beta\alpha}$

$$\begin{aligned} \frac{\nu_{\beta ji}}{\nu_{\alpha ji}} - F_{\beta\alpha} &= \frac{F_{\beta}\delta\langle r^2 \rangle_{ji} + K_{\beta}\mu_{ji}}{F_{\alpha}\delta\langle r^2 \rangle_{ji} + K_{\alpha}\mu_{ji}} - \frac{F_{\beta}}{F_{\alpha}} \\ &= F_{\beta\alpha} \left[\frac{K_{\beta}\mu_{ji}}{F_{\beta}\delta\langle r^2 \rangle_{ji}} - \frac{K_{\alpha}\mu_{ji}}{F_{\alpha}\delta\langle r^2 \rangle_{ji}} \right] \\ &\quad + \mathcal{O} \left[\left(\frac{K_{\alpha}\mu_{ji}}{F_{\alpha}\delta\langle r^2 \rangle_{ji}} \right)^2 \right] \end{aligned} \quad (\text{S4})$$

It is known that mass shifts are smaller than field shifts for heavy elements in general. For the $\alpha = 411$ nm and $\beta = 436$ nm transitions in Yb^+ , the ratio of mass shift and field shift (FS) is $\sim 5\%$ (see table S5). There is even further suppression due to the similar ratio for the transitions α and β , giving a suppression factor $\sim 0.1\%$. The uncertainty in the measured mass of ${}^{168}\text{Yb}$, $1.3\ \mu\text{u}$, corresponds to the uncertainty $\mathcal{O}(1\ \text{kHz})$ in ν_{α} or ν_{β} , and $\mathcal{O}(1\ \text{Hz})$ after the effect on the linear fit is suppressed. The mass uncertainties of the other isotopes $\mathcal{O}(0.01\ \mu\text{u})$ have an effect $\mathcal{O}(10\ \text{mHz})$ on the linear fit. When this level of frequency precision is reached in future precision spectroscopy, it will be necessary to improve the mass measurements.

IV. ESTIMATION OF SYSTEMATIC EFFECTS AND ERRORS

The uncertainties in our measurement are determined directly from the variation of our data points, as described in section II. In the following subsections, we estimate the magnitude of the physical effects we expect to have contributed to this uncertainty, and of any additional systematic shifts. Table S3 summarizes these estimates. Most of the effects discussed here are largely common-mode for the isotope pairs we measure, and produce either zero or very small differential systematic shifts in our measurement (we estimate a total systematic differential shift of $< 10\ \text{Hz}$ - see column 3 in table S3 - which corresponds to $< 10\%$ of our statistical uncertainty). However, we discuss here how drifts over time in experimental parameters lead to uncertainties in these differential shifts (listed in column 3 of table S3); these uncertainties account for most of our measurement error and are seen in the scatter of the data points. For reference, we also list in column 2 of table S3, for each systematic effect, an estimate for the absolute value of the shift it produces on the transition frequency of a single isotope.

A. Second-order Doppler Shift

The fractional Doppler shift to the atomic transition, $\Delta\nu_D/\nu_0$, caused by the motion of the ion in the trap is

given by:

$$\frac{\Delta\nu_D}{\nu_0} = -\cos(\theta)\frac{v}{c} - \frac{v^2}{2c^2} + \mathcal{O}\left(\left(\frac{v}{c}\right)^3\right) \quad (\text{S5})$$

where v is the absolute instantaneous velocity of the ion relative to the lab frame, θ is the angle of observation and ν_0 is the frequency of the atomic transition in the rest frame of the ion.

Since we are in the Lamb-Dicke regime, we can ignore the first term of this equation, the linear Doppler shift, $\frac{v}{c}$, because this term will simply add sidebands to the transition but will not shift the carrier [10].

The second term shifts the atomic transition frequency due to relativistic time dilation. We calculate this term for both micromotion and secular motion of the ion in the trap. Because we are sampling the instantaneous velocity over a time much larger than one oscillation period of the secular or micromotion, we can replace instantaneous velocity by mean square velocity. So the overall fractional second-order Doppler shift is

$$\frac{\Delta\nu_D}{\nu_0} = -\frac{\langle v_s^2 \rangle}{2c^2} + \left(\frac{\Delta\nu}{\nu_0}\right)^{\mu\text{motion}} \quad (\text{S6})$$

where ν_0 is the unshifted transition frequency, $\langle v_s^2 \rangle$ is the mean-square velocity for the secular motion, and $\left(\frac{\Delta\nu}{\nu_0}\right)^{\mu\text{motion}}$ is the micromotion-induced fractional Doppler shift. The secular-motion term can be estimated from the ion's temperature, which we take to be of order the Doppler limit on the 369 nm cooling transition ($\approx 500\mu\text{K}$), giving $\frac{\langle v_s^2 \rangle}{2c^2} \approx 1 \times 10^{-20}$. The micromotion term can be calculated for our trap parameters using Eq. 30 in [11]. We conservatively estimate that the ion experiences a DC field in the trap E of order 50 V/m which gives a micromotion-induced fractional shift of -8×10^{-17} . This dominates over the secular motion shift. From this, we estimate that a small systematic differential second-order Doppler shift of 2 mHz will arise from the mass difference between isotopes. The main source of uncertainty on this differential shift is expected to be temporal drifts in micromotion compensation. If we assume that E can change by around 50 V/m, between measurements of isotope transition frequencies, we arrive at an uncertainty on this differential second-order Doppler shift of $\approx 100\text{mHz}$.

B. Black-body Shift

The black-body radiation (BBR) shifts on the transitions probed here are well approximated by [12]:

$$\Delta\nu_{\text{BBR}} = -\frac{1}{2}\Delta\alpha_0(831.9 \text{ V/m})^2\left(\frac{T}{300 \text{ K}}\right)^4 \quad (\text{S7})$$

where $\Delta\alpha_0$ is the difference in scalar polarizability between the atomic states associated with the transition of interest.

Calculations of the fractional BBR shift for the 436 nm transition in ^{171}Yb have estimated $\Delta\nu_{\text{BBR}} \approx -0.4 \text{ Hz}$ [12, 13]. We assume similar results for the 411 nm transition since the similar orbital wavefunctions of the $^2D_{3/2}$ and $^2D_{5/2}$ states imply that $\Delta\alpha_0$ should be similar for both transitions (the small difference in the wavefunctions arises from the relativistic effect). The main source of a differential BBR shift in our experiment will be temperature drifts. Conservatively, we estimate that the temperature can change by up to 3 K over the course of our shift measurement, which yields a change in $\Delta\nu_{\text{BBR}}$ of $\approx 20 \text{ mHz}$.

C. Electric quadrupole shift

A frequency shift results from the interaction of the quadrupole moment of the electronic state with electric field gradients from the trap. The shift is of order

$$\Delta\nu_{\text{quad}} \sim \frac{\Theta \cdot \nabla E}{h} \quad (\text{S8})$$

The quadrupole moments for the $^2D_{3/2}$ and $^2D_{5/2}$ states of Yb^+ have been calculated to be $2.068(12)\text{ea}_0^2$ and $3.116(15)\text{ea}_0^2$ respectively [14]. Time-varying electric field gradients due to patch potentials on the chip trap can lead to a differential shift between isotopes. We observe a typical day-to-day variation the DC micromotion compensation voltages applied to our trap electrodes of 20 mV. Conservatively, we consider a maximum variation of 200 mV during the course of a shift measurement data-taking run. From this, we infer that differential patch-potential gradients of order $\lesssim 1 \text{ V/mm}^2$ could occur, which would lead to a differential quadrupole shift of $\lesssim 2 \text{ Hz}$.

D. Gravitational red shift

Differential gravitational shifts in the measured isotope transition frequencies could arise from changes in height of the apparatus due to vibrations or thermal expansion over the course of our measurements. Considering the thermal expansion of the building our lab is housed in and typical amplitudes of vibrations of optical table surfaces, we estimate that such height changes should be of order 1 mm, which would lead to a differential shift uncertainty of $\sim 0.1 \text{ mHz}$.

E. Laser-induced AC Stark shifts

1. Off-resonant probe light couplings

Most AC stark shifts in this experiment are common-mode between isotopes, with differential shifts arising only due to laser-intensity drifts and small fractional

frequency differences between the isotopes. The transitions we probe in Yb^+ share the $^2S_{1/2}$ ground state both with far-off-resonant transitions in the atom (e.g. 369 nm transition $^2S_{1/2} \longleftrightarrow ^2P_{1/2}$) and the closer-detuned Zeeman components of probed transition (see Figs. S2, S3). The latter cause significant light shifts, but these are equal and opposite for the each pair of Zeeman-component transitions we measure (i.e. the shift on R is equal and opposite to that on B), and will hence largely cancel out after averaging. Calculated estimates of the light shifts caused by off-resonant coupling of the probe laser are listed in table S2.

We estimate that probe-light intensity fluctuations of order 3% between measurements of each Zeeman transition will lead to uncertainties on the center of order 30 Hz.

We also consider that the probe light intensity can systematically vary by up to 20% when tuned to different isotope transition frequencies. This can lead to a systematic change in the probe-induced AC stark shift for different isotopes. However, this effect is again largely cancelled out since the shift on the two Zeeman transitions we measure are equal and opposite. The remaining systematic shift will hence arise only from any potential deviation from linear polarization of the probe laser beam, which could cause one of the Zeeman transitions to be preferentially driven. This deviation is limited to 1 part in 10^4 by a Glan-Taylor polarizer placed in the probe laser beam path in combination with the effect of the vacuum chamber window. Hence, we estimate a systematic differential light shift of $\lesssim 20$ mHz between isotopes.

2. Non-probe light leakage

AOM leakage of 369-nm light during the probe time of the experiment can shift the $^2S_{1/2}$ ground state of the probed transitions. We estimate the leakage to be ≈ 5 nW (from a $100 \mu\text{W}$, 20 MHz red-detuned beam focused to a beam waist of $75 \mu\text{m}$), which leads to a shift of -1.3×10^3 Hz. Similarly, we estimate that leakage of the 935 nm beam will shift the excited $^2D_{3/2}$ state of the 436 nm probed transition by +440 Hz. Both these shifts are common-mode between isotopes, but intensity drifts of the leaked laser light, estimated to be of order 3%, will contribute an uncertainty of order 30 Hz.

A less significant light shift will also arise from the 935 nm light left on during the 411 nm pulse sequence probe time. The 935 nm beam can also shift the 1070 nm transition connecting the $^2D_{5/2}$ state (excited state of the 411 nm transition) to the $^3D[3/2]_{1/2}$ state (excited state of the 935 nm transition). We estimate this shift to be of order -4×10^{-2} Hz, contributing an uncertainty of ≈ 1 mHz to our measurements.

Finally, a 402 nm laser beam was also used during our experiments to transfer-lock an optical cavity used for increasing the ionization power during ion loading [15]. We estimate that the uncertainty from the AC Stark shift

caused by this laser is < 10 Hz, assuming a maximum intensity drift of 30%.

F. Shift of center of Ramsey fringe by off-resonant Zeeman transitions

The measured Ramsey fringe of a Zeeman transition of interest is perturbed by other Zeeman transitions that are being driven off-resonantly at the same time. The observed signal can be either a sum of different Ramsey fringes, or there may be quantum interference if the off-resonant transition shares a state with the transition of interest. We can estimate the magnitude of the frequency pulling by fitting a sum of different Ramsey fringes.

The maximum size of the pulling is ~ 20 Hz for a detuning ~ 1 MHz. The frequency pulling has opposite sign for symmetric Zeeman transitions R and B and the effect will be cancels out after the frequencies of transition R and B are averaged. The differential shift from intensity fluctuation and asymmetric σ^\pm polarizations is suppressed due to the fact that Ramsey fringes are insensitive to the change in ω_R to the first order. The size of the pulling due to B -field fluctuation can be significant and $O(10)$ Hz is taken as the upper bound of the effect.

G. Micromotional Stark shift

If the ion is shifted off the RF null of the Paul trap by stray DC fields, the RF field it experiences will Stark shift the transitions we probe. This shift is given by [16]

$$\Delta\nu = -\frac{\langle E^2 \rangle}{2\hbar} \left(\Delta\alpha_0 + \frac{1}{2}\alpha_2(3\cos^2\beta - 1) \left[\frac{3m_j^2 - J(J+1)}{J(2J-1)} \right] \right) \quad (S9)$$

where $\langle E^2 \rangle$ is the mean-squared value of the electric field experienced by the ion, β is the angle between the electric field and the quantization axis, $\Delta\alpha_0$ is the difference in the scalar polarizabilities between the ground and excited states of the transition, α_2 is the tensor polarizability of the excited level (the tensor polarizability for the $^2S_{1/2}$ ground state is zero) and J, m_j are the angular momentum quantum numbers for the excited state.

Based on doubling the typical day-to-day variation we observe in micromotion compensation voltages for our trap, we estimate that the stray DC field experienced by the ion to be ≈ 20 V/m. This gives a micromotion amplitude of $A_{\mu\text{m}} = 50$ nm for our trap, which can be translated into an RF electric field amplitude of $E_0 = \frac{m\Omega_{\text{RF}}^2 A_{\mu\text{m}}}{e} \approx 24$ V/m (where Ω_{RF}^2 is the RF drive frequency in for our trap and m is the mass of the Yb^+ isotope). Conservatively, we use here $E_0 = 50$ V/m. From this, and using values for $\Delta\alpha_0$ and α_2 for the $^2D_{3/2}$ level from reference [13], we estimate a micromotional Stark shift of order 1 mHz.

The differential shift between isotopes is expected to be dominated by changes in the stray field landscape in

TABLE S2. Estimated laser-induced AC Stark shifts due to off-resonant couplings of the probe laser.

Off-resonantly driven transition	Estimated Stark shift on 411 nm transition [Hz]	Estimated Stark shift on 436 nm transition [Hz]
369	-1.2×10^2	-2.4×10^2
467	$+5.1 \times 10^{-20}$	$+2.8 \times 10^{-19}$
411	—	-1.1×10^{-3}
436	$+5.5 \times 10^{-5}$	—
B'	$R:-800$	$R:-1160$
R'	$B:+800$	$B:+1160$

the trap during the isotope-shift measurement, and hence we include the full 1mHz in our uncertainty budget for this shift. Note that, even in the absence of stray-field fluctuations, there is a systematic $\approx 2\%$ change in the value of this shift between isotopes since the micromotional Stark shift is proportional to the square of the ion mass.

H. AOM switching-induced phase chirp

Phase shifts in $\frac{\pi}{2}$ -pulses induced when an AOM switches the light are known to cause systematic errors in transition frequencies measured via Ramsey spectroscopy [17, 18]. Ref. [17] reported the shift in transition frequency by 1.6 Hz when the pulse time $\tau = 1.5 \mu s$ and the interrogation time $T = 21.6 \mu s$ are used for 657-nm transition in Ca. As the pulse time in our experiment is longer (which makes the effect smaller), the interrogation time is of the same order of magnitude, and the frequency of the probe light is similar, the effect is expected to be less than $O(1 \text{ Hz})$.

I. Zeeman shifts and absolute frequency stability of the probe light

Both magnetic field drifts and fluctuations in the absolute frequency stability of the probe laser, which we lock to an ultra-low expansion cavity, will lead to frequency shifts of the transitions we probe. Changes in magnetic field that do not occur much faster than the time it takes us to scan over a given Zeeman-component (on the order of a few minutes) should lead to oppositely-signed linear shifts on the measured frequency of Zeeman components symmetrically detuned from the transition center. We focus this discussion on linear Zeeman shifts since, at our magnetic field of 1.1 G, for ions with no hyperfine structure like the even Yb⁺ isotopes we measure here, the quadratic Zeeman shift is expected to be of order 100 mHz [19], significantly smaller than the linear shift (based on the measured current noise in our magnetic-field coils, we estimate that our magnetic-field noise is $\lesssim 0.1\%$, giving an uncertainty on the quadratic Zeeman shift of 0.2 mHz.).

To ascertain whether B-field drifts contributed significantly to the spread in our measured transition centers, we performed measurements of the center using Zeeman components of the excited state with larger B-field sensitivity. We found no significant change in the spread of the data when more B-field sensitive Zeeman states were used. Hence, we conclude that linear Zeeman shifts do not contribute significantly to the point-to-point frequency shifts we observe in our experiment; we estimate here a contribution of the order of 300 Hz (before averaging over repeated measurements).

The main contribution to our observed point-to-point frequency drifts derives from fluctuations in the absolute stability of the probe laser locked to the ULE cavity. Residual Amplitude Modulation (RAM) effects from the EOM used for this laser's PDH lock produce a common-mode shift on the measured frequency opposing Zeeman components of the probed transition. As well as RAM, thermal drifts of the cavity due to intracavity light also contribute to fluctuations in the probe laser's absolute frequency stability. We estimate that these effects lead to point-to-point frequency shifts of $\sim 1 \text{ kHz}$ in our experiment. This is our largest source of uncertainty, but it is reduced by repeated averaging to a level consistent with the $\sim 300 \text{ Hz}$ -spread we observe in our final data that is included in the quoted statistical error.

V. CALCULATION OF PARAMETERS ASSOCIATED WITH ATOMIC WAVEFUNCTIONS

To evaluate quantities like K_α , F_α , G_α , and D_α appearing in Eq. 1 in the main text, the change in the distribution of electrons in Yb⁺ over space during the transitions of interest needs to be known. In particular, it is crucial to obtain $D_{\beta\alpha}$ to translate the measured nonlinearity into a new-boson-mediated neutron-electron coupling constant $y_e y_n$. Atomic structure calculations have been developed to numerically study electronic structures of atoms, and have been carried out here using some of the methods in the field as described in section V A.

TABLE S3. Estimated contributions to measurement error. Since we measure differences between transition frequencies of pairs of isotopes, only differential shifts affect our measurement, but absolute shifts are also listed here for reference (column 2). The main contributions to our measurement error come from uncertainties on the differential shifts (column 3), which arise mainly from temporal drifts in experimental parameters between measurements of different isotopes (the systematic differential shifts listed here are estimated for next-neighboring isotopes). The uncertainties listed in column 3 are per measured data point (i.e. if the isotope shift were inferred from a single measurement of the transition center in each isotope). For the dominant shifts, we also provide an estimate of the uncertainty after averaging over ten measurements of the center (for most shift measurements, we perform 15 measurements of the transition center but, for measurements involving the 168 isotope, we perform only 10 repeats due to the long loading times required for this isotope). The estimation of the errors listed in this table is detailed in the text (section IV).

	Estimated Shift [Hz]	Magnitude of Absolute Shift [Hz]	Estimated Differential Shift [Hz]
Second-order Doppler Shift	$5 \times 10^{-2} \pm 1 \times 10^{-1}$	$2 \times 10^{-3} \pm 1 \times 10^{-1}$	
Black-body shift	$4 \times 10^{-1} \pm 2 \times 10^{-2}$	$0 \pm 2 \times 10^{-2}$	
Electric quadrupole shift	$2 \times 10^0 \pm 2 \times 10^0$	$0 \pm 2 \times 10^0$	
Gravitational redshift	$1 \times 10^{-2} \pm 1 \times 10^{-4}$	$0 \pm 1 \times 10^{-4}$	
Laser-induced Stark shift	$1 \times 10^{-1} \pm 4 \times 10^1$	$2 \times 10^{-2} \pm 4 \times 10^1$	
Micromotional Stark shift	$2 \times 10^{-1} \pm 1 \times 10^{-3}$	$2 \times 10^{-5} \pm 1 \times 10^{-3}$	
Quadratic Zeeman shift	$1 \times 10^{-1} \pm 2 \times 10^{-4}$	$0 \pm 2 \times 10^{-4}$	
AOM-induced phase chirp	$0 \pm O(1 \text{ Hz})$	$0 \pm O(1 \text{ Hz})$	
Linear Zeeman shift	$0 \pm 3 \times 10^2$	$0 \pm 3 \times 10^2$ ($\sim 1 \times 10^2$ after averaging)	
Absolute frequency stability of PDH-locked probe laser	$0 \pm 1 \times 10^3$	$0 \pm 1 \times 10^3$ ($\sim 3 \times 10^2$ after averaging)	

A. Description of methods

Here, the Dirac-Hartree-Fock (DHF) method [20, 21] followed by the configurational interaction (CI) method [22–25] has been used to calculate the two transitions in Yb^+ . The calculation is relatively reliable because there is only one valence electron. Nevertheless, the full electron calculation is required to obtain the perturbed core-electron wavefunction due to the change in the valence-electron state; the change in core s orbitals gives the major contribution to the sensitivity of $y_e y_n$ in the high- m_ϕ regime ($\gtrsim 1$ MeV). More advanced methods, for instance CI combined with many-body perturbation theory (CI+MBPT) [26–28] and CI+All-order method [12, 29], have been developed. The calculation with the MBPT method (not combined with CI method) has been performed independently, and the results are compared in section V B, as well as the main text, to provide an estimate of the systematic uncertainty of the calculation.

The DHF and CI calculation were done with GRASP2018 [30]. The DHF for closed core, from $1s$ to $5p$ subshells, was calculated first to obtain the basis set for core electrons. Then a valence electron was added and the basis set for all electrons was calculated. Finally, the correlation orbitals were added layer by layer to get better accuracy by taking core-core and core-valence correlation effects into account, and achieve convergence. CI calculations followed.

Once the wavefunctions were obtained, the change in radial electron density functions $\rho_\alpha(r)$ [31] during transition α was calculated from the wavefunctions (it is not a part of GRASP2018), and all wavefunction-dependent quantities were obtained from the electron

density $\rho_\alpha(r)$'s.

The software package RIS4 [32] was used to calculate K_α from the outputs of GRASP2018. The details of the method by which this is achieved can be found in Ref. [32].

The Seltzer moment expansion relates field shifts and the expansion of $\rho_\alpha(r)$ at the origin [33–35]:

$$\rho_\alpha(r) = r^2 \left[\xi_\alpha^{(0)} + \xi_\alpha^{(2)} r^2 + \dots \right] \quad (\text{S10})$$

$$\nu_{\alpha ji}^{\text{FS}} = \sum_{k=0}^{\infty} \underbrace{\frac{c\alpha' Z}{2\pi}}_{F_\alpha^{(k)}} \frac{\xi_\alpha^{(k)}}{(k+2)(k+3)} \delta \langle r^{k+2} \rangle \quad (\text{S11})$$

where $\alpha' \approx 1/137$ in Eq. S11 is the fine-structure constant and Z is the proton number. $F_\alpha \equiv F_\alpha^{(0)}$ and $G_\alpha^{(4)} \equiv F_\alpha^{(2)}$ in our notation. $\xi_\alpha^{(0)}$ and $\xi_\alpha^{(2)}$ obtained by fitting $\rho_\alpha(r)$ with a power series at the origin can be converted into F_α and $G_\alpha^{(4)}$, respectively.

The shift in transition frequency due to a new boson $\nu_{\alpha ji}^\phi = \langle a_{ji} V_{ne}(r) \rangle_\alpha / \hbar = v_{ne} D_\alpha a_{ji}$ (all quantities are defined in the main text) gives an expression for D_α :

$$D_\alpha(m_\phi) = \frac{c}{2\pi} \int_0^\infty dr \rho_\alpha(r) \frac{e^{-m_\phi r c / \hbar}}{r}. \quad (\text{S12})$$

The numerical calculation of D_α for a given $\rho_\alpha(r)$ and m_ϕ is straightforward.

The quadratic FS (QFS) $G_\alpha^{(2)}[\delta \langle r^2 \rangle^2]$ captures the change in wavefunction itself due to the change in nuclear size, which is illustrated in the expression for the

electronic factor:

$$G_{\alpha}^{(2)} = \frac{1}{2} \frac{\partial F_{\alpha}}{\partial \langle r^2 \rangle} = \frac{c\alpha' Z}{24\pi} \frac{\partial \xi_{\alpha}^{(0)}}{\partial \langle r^2 \rangle} \quad (\text{S13})$$

$G_{\alpha}^{(2)}$ is given as the rate of change in electron density at the origin as nuclear size changes, and evaluating it requires repeated atomic structure calculations while gradually varying the nuclear size.

The electronic factors were also calculated using an independent method that combines Brueckner MBPT and the random phase approximation (RPA) [36] implemented in AMBiT [37]. The MBPT correction accounting for core-valence correlations was calculated to second order in the residual Coulomb interaction. This was written in terms of a non-local potential $\hat{\Sigma}$, which was then added to the Dirac-Fock potential and solved self consistently to give “Brueckner” valence orbitals and energies. The Yukawa matrix elements for individual levels were calculated directly using the overlap of the orbitals and the Yukawa operator. The Yukawa potential also polarises the core, and this effect is included using the random-phase approximation. The D_{α} (or D_{β}) is obtained by subtracting the Yukawa matrix elements of the corresponding levels in the transition α (or β). To obtain $G_{\alpha(\beta)}^{(4)} = \partial \nu_{\alpha(\beta)} / \partial \langle r^4 \rangle$, the calculation for transition $\alpha(\beta)$ is repeated while changing the nuclear charge distribution in such a way that $\langle r^4 \rangle$ changes but $\langle r^2 \rangle$ is constant. Similarly, to obtain $G_{\alpha(\beta)}^{(2)} = \frac{1}{2} \partial^2 \nu_{\alpha(\beta)} / (\partial \langle r^2 \rangle)^2$, the calculation is repeated while changing $\langle r^2 \rangle$ but keeping $\langle r^4 \rangle$ constant.

B. Comparison of calculations with experimental results

The accuracy of the calculated wavefunction using CI and MBPT methods is checked against our experimental data and literature values. The results are summarized in table I, table S4, table S5, and Fig. S10.

1. Difference in the second nuclear charge moment $\delta \langle r^2 \rangle$

The nuclear parameters $\lambda_{\alpha ji}$ [33, 34, 41, 42], which are essentially $\delta \langle r^2 \rangle_{ji}$, can be obtained by dividing the measured FS, $F_{\alpha} \lambda_{\alpha ji}$, by the calculated F_{α} . The FS $F_{\alpha} \lambda_{\alpha ji}$ can be obtained by subtracting $K_{\alpha} \mu_{ji}$ from the measured isotope shifts $\nu_{\alpha ji}$ (K_{α} is derived from the wavefunction calculation and μ_{ji} from mass spectroscopy [8, 43, 44]). In short,

$$\lambda_{\alpha ji} = \frac{\nu_{\alpha ji}^{\text{FS}}}{F_{\alpha}} = \frac{\nu_{\alpha ji} - K_{\alpha} \mu_{ji}}{F_{\alpha}}. \quad (\text{S14})$$

Plugging Eq. S11 into Eq. S14 gives

$$\lambda_{\alpha ji} = \delta \langle r^2 \rangle_{ji} \left[1 + \frac{G_{\alpha}^{(4)}}{F_{\alpha}} \frac{\delta \langle r^4 \rangle_{ji}}{\delta \langle r^2 \rangle_{ji}} + \dots \right] \quad (\text{S15})$$

TABLE S4. Quantities calculated using CI and MBPT methods, and estimated from the experiment for α : 411 nm and β : 436 nm transitions. $f_{\alpha, \beta} = \omega_{\alpha, \beta} / (2\pi)$ are the transition frequencies. Other quantities are defined in the main text.

		CI	MBPT	Exp.
f_{α}	[THz]	808.11	764.86	729.47 ^{a b}
f_{β}	[THz]	770.13	717.94	688.36 ^{a c}
F_{α}	[GHz/fm ²]	-15.852	-16.570	
F_{β}	[GHz/fm ²]	-16.094	-16.771	
$F_{\beta\alpha}$		1.0153	1.0121	1.01141024(86)
K_{α}	[GHz·u]	-1678.3		
K_{β}	[GHz·u]	-1638.5		
$K_{\beta\alpha}$	[GHz·u]	65		120.208(23)
$G_{\alpha}^{(2)}$	[MHz/fm ⁴]	40.23	43.47	
$G_{\beta}^{(2)}$	[MHz/fm ⁴]	41.44	44.22	
$G_{\beta\alpha}^{(2)}$	[kHz/fm ⁴]	232	-36	59(17) ^d
$G_{\alpha}^{(4)}$	[MHz/fm ⁴]	14.9291	10.338(3) ^e	
$G_{\beta}^{(4)}$	[MHz/fm ⁴]	15.1532	10.564(3) ^e	
$G_{\beta\alpha}^{(4)}$	[kHz/fm ⁴]	-3.5	-5(5) ^e	
D_{α}^{f}	[THz]	44145	40189	
D_{β}^{f}	[THz]	48419	47962	
$D_{\beta\alpha}^{\text{f}}$	[THz]	3602	6909	

^a The exact value varies by the few-GHz isotope shifts.

^b Ref. [6, 38]

^c Ref. [39, 40]

^d If the observed nonlinearity comes purely from $G_{\beta\alpha}[\delta \langle r^2 \rangle^2]$.

^e Numerical noise estimates

^f At $m_{\phi} = 1$ eV. Values over different m_{ϕ} ’s are shown in Fig. S10.

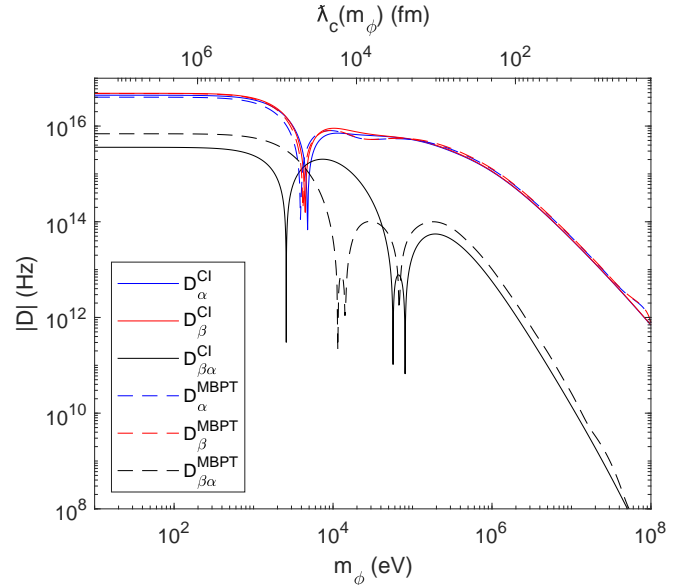


FIG. S10. Electronic factors associated with new-boson coupling D_{α} , D_{β} , and $D_{\beta\alpha}$ vs. boson mass m_{ϕ} (bottom) and reduced Compton wavelength (top) for α = 411 nm and β = 436 nm transitions. The solid lines are for the CI calculation, and the dashed lines for the MBPT calculation. D_{α} , D_{β} , and $D_{\beta\alpha}$ are positive at $m_{\phi} = 1$ eV and change their signs at the peaks.

To obtain $\delta\langle r^2 \rangle$, the contribution of higher-order moments should be subtracted from $\lambda_{\alpha ji}$. Plugging Eq. S23 into Eq. S15 gives

$$\lambda_{\alpha ji} = \delta\langle r^2 \rangle_{ji} \left[1 + 2b \frac{G_\alpha^{(4)} \langle r^2 \rangle_l}{F_\alpha} \left(1 + \frac{\delta\langle r^2 \rangle_{jl} + \delta\langle r^2 \rangle_{il}}{2\langle r^2 \rangle_l} \right) \right] \quad (\text{S16})$$

$$+ O(\delta\langle r^6 \rangle) \\ \approx \delta\langle r^2 \rangle_{ji} \left[1 + 2b \frac{G_\alpha^{(4)} \langle r^2 \rangle_l}{F_\alpha} \right] \quad (\text{S17})$$

where l refers to some fixed isotope (here $l = 172$). Using the values of F_α and $G_\alpha^{(4)}$ in table S4, the value of b for Yb in table S6, and $\langle r^2 \rangle_l = 28.02(1)$ fm 2 from Ref. [41], the correction is calculated to be -6.97%. The values from the CI calculation are used as they give the ratios $G_\alpha^{(4)}/F_\alpha = -9.418 \times 10^{-4}$ fm $^{-2}$ and $G_\beta^{(4)}/F_\beta = -9.416 \times 10^{-4}$ fm $^{-2}$, which are closer to the value given in a seminal paper about the Seltzer moment expansion: -9.29×10^{-4} fm $^{-2}$ [33, 41] (this is approximately the universal across the levels and the transitions in a species of atom; see Ref. [33].). The value of b is assumed to vary less than about 1% between the Yb isotopes (see table S6). The contribution of the term involving $\delta\langle r^2 \rangle_{jl} + \delta\langle r^2 \rangle_{il} \lesssim 0.4$ fm 2 in Eq. S16 is $\lesssim 0.8\%$ of the -6.97% correction from $\delta\langle r^2 \rangle$. Therefore, the conversion from $\lambda_{\alpha ji}$ to $\delta\langle r^2 \rangle$ via Eq. S17 is precise to 0.1%, unless the contribution of higher-order moments $\delta\langle r^{k>4} \rangle$ is larger than 0.1%.

The calculated mass shift, field shift, and $\delta\langle r^2 \rangle$ values are shown in Table S5. The calculated $\delta\langle r^2 \rangle$'s are in good agreement with the values in Ref. [42], with differences of less than 10%. $\delta\langle r^2 \rangle$ values obtained by using F_α and F_β from the CI and MBPT calculations are compared in the table. For the analyses that use $\delta\langle r^2 \rangle$ (e.g., the QFS line in Fig. 3), the values of $\delta\langle r^2 \rangle$ that involve MBPT calculation are used, since the MBPT method is expected to better capture valence-core electron correlation. Note that, however, any difference in F_α or F_β will change only the overall scale of $\delta\langle r^2 \rangle$ values of different isotopes (see Eqs. S14 and S17). Such differences would not change the pattern of nonlinearity originating from $\delta\langle r^2 \rangle_{ji}$, or the direction of the QFS line in Fig. 3a.

2. Slope and y -intercept in King plot

The slope and y -intercept $F_{\beta\alpha}$ and $K_{\beta\alpha}$ in the (standard) King plot can be obtained from the calculated F_α , F_β , K_α , and K_β , as defined in the main text. The calculated slopes $F_{\beta\alpha}^{\text{CI}}$ and $F_{\beta\alpha}^{\text{MBPT}}$ show excellent agreement with the experimental value of $F_{\beta\alpha}^{\text{exp}}$, while the y -intercept $K_{\beta\alpha}^{\text{CI}}$ is of the same order as the experimental value $K_{\beta\alpha}^{\text{exp}}$ (see the main text or table S4). Note, however, that the calculation of the mass shift coefficient is known to be a challenging task [45, 46]. We note that $K_{\beta\alpha}$ is the

marginal remainder after K_β and K_α for the two D states with very similar wavefunctions are mostly cancelled out (at the level of 96%). Therefore, the disagreement of the calculated $K_{\beta\alpha}$ to the experimental value does not necessarily imply the departure of the mass shift coefficients of each transition K_α or K_β from their true values by the same factor.

F_α is determined by the value of the wavefunctions at the origin (Eq. S11). Therefore, the good agreement of $\delta\langle r^2 \rangle$ and $F_{\beta\alpha}$ with the experimental values implies that the calculated wavefunctions are reliable near the origin, the region which provides the dominant contribution to the sensitivity to y_{eyn} in the high- m_ϕ regime.

C. Estimation of nonlinearities within the SM

The dominant SM contributions to the nonlinearity are expected to originate from higher-order FS terms,

$$\delta\nu_\alpha^{(2)} = G_\alpha^{(2)} [\delta\langle r^2 \rangle^2] + G_\alpha^{(4)} \delta\langle r^4 \rangle \quad (\text{S18})$$

$$= G_\alpha [\delta\langle r^2 \rangle^2] \quad (\text{S19})$$

where $G_\alpha = G_\alpha^{(2)} + bG_\alpha^{(4)}$ is the effective QFS electronic factor (see Eq. S21 for b), as the higher-order terms in mass shift, $\alpha^2(m/M)^2$, are negligibly small [47]. The first term in Eq. S18 (QFS) is from the second-order perturbation of the FS (Eq. S13), while the second term is the second leading-order moment in the Seltzer expansion for the first-order perturbation of the FS (Eq. S11). The correlation between $\langle r^4 \rangle$ and $\langle r^2 \rangle^2$ in Eq. S21 gives the next relation Eq. S19 (see below in this section), and the two effects are combined with the same nuclear factor $[\delta\langle r^2 \rangle^2]$. The contribution of this effective QFS to the nonlinearity is given as

$$G_{\beta\alpha} [\delta\langle r^2 \rangle^2] = [G_\beta - F_{\beta\alpha} G_\alpha] [\delta\langle r^2 \rangle^2] \\ = G_{\beta\alpha}^{(2)} [\delta\langle r^2 \rangle^2] + bG_{\beta\alpha}^{(4)} [\delta\langle r^2 \rangle^2] \quad (\text{S20})$$

and the contributions from the QFS and the fourth-order Seltzer moment can be estimated separately.

For the QFS, We calculate $G_\alpha^{(2)} = 40.23$ MHz/fm 4 and $G_\beta^{(2)} = 41.44$ MHz/fm 4 for the $\alpha = 411$ nm and $\beta = 436$ nm transitions, respectively, using the CI calculation as in table S4. For the fourth-order Seltzer moment, $G_\alpha^{(4)}$ and $G_\beta^{(4)}$ were calculated to be 14.9291 MHz/fm 4 and 15.1532 MHz/fm 4 . The F_α and $G_\alpha^{(4)}$ are highly correlated (i.e., $F_\beta/F_\alpha \approx G_\beta^{(4)}/G_\alpha^{(4)}$), which suppresses $G_{\beta\alpha}^{(4)}$ by a factor of $\sim 2 \times 10^4$, giving $G_{\beta\alpha}^{(4)} = -3.5$ kHz/fm 4 , while the suppression for the QFS is ~ 200 , yielding $G_{\beta\alpha}^{(2)} = 232$ kHz/fm 4 . The different suppression makes the contribution of QFS to the nonlinearity much bigger (by a factor of ~ 66) than that of fourth-order Seltzer moment although $G_\alpha^{(4)}$ is smaller than $G_\alpha^{(2)}$ only by a factor ~ 2.7 .

TABLE S5. Mass shifts, field shifts and nuclear charge radius difference $\delta\langle r^2 \rangle$ from measured isotope shifts and coefficients K , F from atomic-structure calculation in table S4 for transitions α : 411 nm and β : 436 nm.

Isotope pairs	$K\mu_{ji}$ [MHz]		$F\lambda_{ji}$ [MHz]		CI		$\delta\langle r^2 \rangle$ [fm ²]		Ref. [42] ^a
	(j,i)	α	β	α	β	α	β	α	β
(168,170)	-117.7	-114.9	2297	2327	-0.156	-0.155	-0.149	-0.149	-0.1561(3)
(170,172)	-115.0	-112.2	2160	2189	-0.146	-0.146	-0.140	-0.140	-0.1479(1)
(172,174)	-112.4	-109.7	1695	1719	-0.115	-0.115	-0.110	-0.110	-0.1207(1)
(174,176)	-109.9	-107.3	1619	1641	-0.110	-0.110	-0.105	-0.105	-0.1159(1)

^a Only statistical errors are presented in the parentheses. The large systematic errors in the electronic factors are not taken into account.

The nuclear factor $[\delta\langle r^2 \rangle]^2 \lesssim 0.07$ fm⁴ gives $G_{\beta\alpha}[\delta\langle r^2 \rangle]^2 \lesssim 15$ kHz. The out-of-plane components of $[\delta\langle r^2 \rangle]^2$ are $\lesssim 0.025$ fm⁴ and thus the nonlinearity is the order of $\lesssim 5$ kHz.

To justify Eq. S19 that absorbs the shape FS term $\delta\langle r^4 \rangle$ into an effective QFS $(\delta\langle r^2 \rangle)^2$, we note that we expect the correlation

$$\langle r^4 \rangle_i = b\langle r^2 \rangle_i^2 \quad (\text{S21})$$

to hold to a good approximation, where $b \approx 1$ is identical over different isotopes. This equation implies that the *shape* of the charge distribution is preserved while the size varies between different isotopes: $\rho_{n,j}(r) = \rho_{n,i}(r/\epsilon_{ji})/\epsilon_{ji}$. Eq. S21 is expected to hold for heavy ions in the absence of shell effects to order $1/A$ or better, where A is the atomic mass. From Eq. S21, one obtains the relation between $\delta\langle r^4 \rangle$ and $\delta\langle r^2 \rangle$ as follows:

$$\begin{aligned} \delta\langle r^4 \rangle_{il} &= \langle r^4 \rangle_i - \langle r^4 \rangle_l \\ &= b [\langle r^2 \rangle_i^2 - \langle r^2 \rangle_l^2] \\ &= b [\langle r^2 \rangle_l + \delta\langle r^2 \rangle_{il}]^2 - \langle r^2 \rangle_l^2 \\ &= b [2\langle r^2 \rangle_l \delta\langle r^2 \rangle_{il} + (\delta\langle r^2 \rangle_{il})^2] \end{aligned} \quad (\text{S22})$$

where $\langle r^n \rangle_l$ is for a fixed reference isotope l . Consequently,

$$\begin{aligned} \delta\langle r^4 \rangle_{ji} &= \delta\langle r^4 \rangle_{jl} - \delta\langle r^4 \rangle_{il} \\ &= b [2\langle r^2 \rangle_l \delta\langle r^2 \rangle_{ji} + [\delta\langle r^2 \rangle]^2_{ji}] \\ &= 2b\langle r^2 \rangle_l \delta\langle r^2 \rangle_{ji} \left[1 + \frac{\delta\langle r^2 \rangle_{jl} + \delta\langle r^2 \rangle_{il}}{2\langle r^2 \rangle_l} \right] \end{aligned} \quad (\text{S23})$$

where $[\delta\langle r^2 \rangle]^2_{ji} \equiv (\delta\langle r^2 \rangle_{ji})^2 - (\delta\langle r^2 \rangle_{il})^2$. The last two rows show that $\delta\langle r^4 \rangle$ is nearly linear in $\delta\langle r^2 \rangle$ for small change in size ($\delta\langle r^2 \rangle_{jl}, \delta\langle r^2 \rangle_{il} \ll \langle r^2 \rangle_l$), and the nonlinearity is due to $[\delta\langle r^2 \rangle]^2$. The linear term $2b\langle r^2 \rangle_l \delta\langle r^2 \rangle_{ji}$ is absorbed into the leading-order FS $F_\alpha\langle r^2 \rangle$, while the nonlinear term is combined with the QFS: $(G_\alpha^{(2)} + bG_\alpha^{(4)})[\delta\langle r^2 \rangle]^2_{ji}$.

The assumption Eq. S21 can be tested using the nuclear charge distribution $\rho_n(r)$ measured by electron scattering experiments [48, 49]. The Fourier-Bessel coefficients in Ref. [48] are used to retrieve $\rho_n(r)$ of each isotope and $\langle r^2 \rangle, \langle r^4 \rangle$, and b are calculated using the $\rho_n(r)$.

TABLE S6. $\langle r^4 \rangle$ -to- $\langle r^2 \rangle^2$ ratio b (in Eq. S21) for the isotopes of Pd, Sm, and Pb calculated using electron scattering data [48]. The fractional variation $\Delta b/\bar{b}$, the standard deviation of the b coefficients divided by their mean, is shown in the last column for each element. b of ^{174}Yb from the electron scattering data in [49] is shown for comparison.

Element	Isotope	b	$\Delta b/\bar{b}$
Pd	104	1.3173	0.0026
	106	1.3225	
	108	1.3247	
	110	1.3246	
Sm	144	1.2861	0.0129
	148	1.2979	
	150	1.3175	
	152	1.3212	
	154	1.3254	
Pb	204	1.2755	0.0011
	206	1.2735	
	207	1.2770	
	208	1.2758	
Yb	174	1.3211	

The results for Pd, Sm, and Pb are listed in table S6. The variations of b over different isotopes are indeed small: 0.1 to 1%. The difference may be merely due to the experimental uncertainty of the data in Ref. [48].

Finally, note that the choice of l in the definition of $[\delta\langle r^2 \rangle]^2_{ji}$ does not change the associated nonlinearity, as shown below:

$$\begin{aligned} [\delta\langle r^2 \rangle]^2_{ji} &\equiv (\delta\langle r^2 \rangle_{jl})^2 - (\delta\langle r^2 \rangle_{il})^2 \\ &= (\delta\langle r^2 \rangle_{jm} + \delta\langle r^2 \rangle_{ml})^2 - (\delta\langle r^2 \rangle_{im} + \delta\langle r^2 \rangle_{ml})^2 \\ &= [\delta\langle r^2 \rangle]^2_{jm} + 2\delta\langle r^2 \rangle_{ml}\delta\langle r^2 \rangle_{ji} \end{aligned} \quad (\text{S24})$$

where l, m are some fixed isotopes. The last term in Eq. S24 is proportional to $\delta\langle r^2 \rangle_{ji}$ and is readily absorbed into the field shift term.

In summary, the QFS $G_{\beta\alpha}^{(2)}[\delta\langle r^2 \rangle]^2$ gives the dominant contribution to the SM nonlinearity unless the shape of nuclear charge distribution varies strongly between different isotopes. The contributions from other nuclear effects that are not considered here are smaller, e.g., the nuclear polarizability that is expected to contribute at the level < 10 Hz) [50].

VI. GENERALIZATION OF NONLINEARITY MEASURES TO MORE ISOTOPES AND TRANSITIONS

The nonlinearity measures ζ_{\pm} can be generalized for more than 4 pairs of isotopes or more than two transitions. For N pairs of isotopes (i.e. $N + 1$ isotopes), $N - 2$ independent parameters characterizing the pattern of nonlinearity can be defined, and visualized in an $(N - 2)$ -dimensional plot. This can be easily understood with a vectorial approach. Let $\vec{x} = (x_{j_1 i_1}, \dots, x_{j_N i_N})$ where $x_{j_q i_q}$ is a term in Eq. 3 (e.g., $G_{\beta\alpha} \overline{[\delta\langle r^2 \rangle^2]}_{j_q i_q}$) for the q -th isotope pair. After the components along the *King vectors* $\vec{\mu} = (1, \dots, 1)$ (mass shift) and $\vec{\nu}_{\alpha} = (\overline{\nu}_{\alpha j_1 i_1}, \dots, \overline{\nu}_{\alpha j_N i_N})$ (field shift) are sub-

tracted from \vec{x} via linear fitting, the remaining vector can be uniquely determined by the components of $(N - 2)$ vectors $\{\vec{\zeta}_1, \dots, \vec{\zeta}_{N-2}\}$ which are linearly independent from each other and from $\{\vec{\mu}, \vec{\nu}_{\alpha}\}$.

A generalization for more than two transitions can be obtained by pairing transitions; $M - 1$ independent pairs of transitions can be formed out of M transitions and the analysis with a two-dimensional King plot described throughout the paper can be applied to each pair. The nonlinearity measures ζ_{\pm} (or $(\zeta_1, \dots, \zeta_{N-2})$ for the case of $N + 1$ isotopes) from each pair of transitions can be displayed in the same two-dimensional (or $(N - 2)$ -dimensional) plot. In particular, if all of the transition pairs share a certain transition α (i.e., the pairs are $(\alpha, \beta), (\alpha, \gamma), (\alpha, \delta), \dots$), the King vectors $\{\vec{\mu}, \vec{\nu}_{\alpha}\}$ are the same for all pairs of transitions and comparing the nonlinearities becomes straightforward.

[1] M. Cetina *et al.*, *Hybrid approaches to quantum information using ions, atoms and photons*, Ph.D. thesis, Massachusetts Institute of Technology (2011).

[2] S. Olmschenk, K. C. Younge, D. L. Moehring, D. N. Matsukevich, P. Maunz, and C. Monroe, Manipulation and detection of a trapped Yb^+ hyperfine qubit, *Phys. Rev. A* **76**, 052314 (2007).

[3] A.-M. Mårtensson-Pendrill, D. S. Gough, and P. Hannaford, Isotope shifts and hyperfine structure in the 369.4-nm $6s-6p_{1/2}$ resonance line of singly ionized ytterbium, *Phys. Rev. A* **49**, 3351 (1994).

[4] T. Feldker, H. Fürst, N. V. Ewald, J. Joger, and R. Gerritsma, Spectroscopy of the $^2S_{1/2} \rightarrow ^2P_{3/2}$ transition in Yb II: Isotope shifts, hyperfine splitting, and branching ratios, *Physical Review A* **97**, 10.1103/physreva.97.032511 (2018).

[5] K. Sugiyama, A. Wakita, and A. Nakata, Diode-laser-based light sources for laser cooling of trapped Yb^+ ions, in *Conference on Precision Electromagnetic Measurements. Conference Digest. CPEM 2000 (Cat. No. 00CH37031)* (IEEE, 2000) pp. 509–510.

[6] P. Taylor, M. Roberts, S. V. Gateva-Kostova, R. B. M. Clarke, G. P. Barwood, W. R. C. Rowley, and P. Gill, Investigation of the $^2S_{1/2}-^2D_{5/2}$ clock transition in a single ytterbium ion, *Phys. Rev. A* **56**, 2699 (1997).

[7] C. Gerz, J. Roths, F. Vedel, and G. Werth, Lifetime and collisional depopulation of the metastable $5D_{3/2}$ -state of Yb^+ , *Zeitschrift für Physik D Atoms, Molecules and Clusters* **8**, 235 (1988).

[8] R. Rana, M. Höcker, and E. G. Myers, Atomic masses of strontium and ytterbium, *Phys. Rev. A* **86**, 050502 (2012).

[9] Chapter 9: Regression models in B. Efron and R. Tibshirani, *An Introduction to the Bootstrap*, 1st ed. (Chapman & Hall/CRC, New York, 1993). *Bootstrapping pairs* was used, see Chapter 9.5 in the book.

[10] I. Lizuain, J. G. Muga, and J. Eschner, Motional frequency shifts of trapped ions in the Lamb-Dicke regime, *Phys. Rev. A* **76**, 033808 (2007).

[11] D. J. Berkeland, J. D. Miller, J. C. Bergquist, W. M. Itano, and D. J. Wineland, Minimization of ion micro-motion in a paul trap, *Journal of Applied Physics* **83**, 5025 (1998).

[12] M. S. Safranova, M. G. Kozlov, and C. W. Clark, Black-body radiation shifts in optical atomic clocks, *IEEE transactions on ultrasonics, ferroelectrics, and frequency control* **59**, 439 (2012).

[13] A. Roy, S. De, B. Arora, and B. K. Sahoo, Accurate determination of black-body radiation shift, magic and tune-out wavelengths for the $6S_{1/2} \rightarrow 5D_{3/2}$ clock transition in Yb^+ , *Journal of Physics B: Atomic, Molecular and Optical Physics* **50**, 205201 (2017).

[14] D. K. Nandy and B. K. Sahoo, Quadrupole shifts for the $^{171}\text{Yb}^+$ ion clocks: Experiments versus theories, *Phys. Rev. A* **90**, 050503 (2014).

[15] M. Cetina, A. Bylinskii, L. Karpa, D. Gangloff, K. M. Beck, Y. Ge, M. Scholz, A. T. Grier, I. Chuang, and V. Vuletić, One-dimensional array of ion chains coupled to an optical cavity, *New Journal of Physics* **15**, 053001 (2013).

[16] P. Dubé, A. A. Madej, Z. Zhou, and J. E. Bernard, Evaluation of systematic shifts of the $^{88}\text{Sr}^+$ single-ion optical frequency standard at the 10^{-17} level, *Phys. Rev. A* **87**, 023806 (2013).

[17] C. Degenhardt, T. Nazarova, C. Lisdat, H. Stoehr, U. Sterr, and F. Riehle, Influence of chirped excitation pulses in an optical clock with ultracold calcium atoms, *IEEE Transactions on Instrumentation and Measurement* **54**, 771 (2005).

[18] C. Sanner, N. Huntemann, R. Lange, C. Tamm, and E. Peik, Autobalanced ramsey spectroscopy, *Phys. Rev. Lett.* **120**, 053602 (2018).

[19] T. C. M. Niels, and K. Martina, *Trapped Charged Particles: A Graduate Textbook With Problems And Solutions*, Advanced Textbooks In Physics (World Scientific Publishing Company, 2016) p. 388.

[20] I. Grant, B. McKenzie, P. Norrington, D. Mayers, and N. Pyper, An atomic multiconfigurational Dirac-Fock package, *Computer Physics Communications* **21**, 207 (1980).

[21] K. Dyall, I. Grant, C. Johnson, F. Parpia, and E. Plummer, GRASP: A general-purpose relativistic atomic structure program, Computer Physics Communications **55**, 425 (1989).

[22] P. Jönsson, A. Ynnerman, C. Froese Fischer, M. R. Godefroid, and J. Olsen, Large-scale multiconfiguration hartree-fock and configuration-interaction calculations of the transition probability and hyperfine structures in the sodium resonance transition, Phys. Rev. A **53**, 4021 (1996).

[23] S. G. Porsev, M. G. Kozlov, and D. Reimers, Transition frequency shifts with fine-structure constant variation for Fe I and isotope-shift calculations in Fe I and Fe II, Phys. Rev. A **79**, 032519 (2009).

[24] B. Fawcett and M. Wilson, Computed oscillator strengths, landé g values, and lifetimes in Yb II, Atomic Data and Nuclear Data Tables **47**, 241 (1991).

[25] E. Biémont, J.-F. Dutrieux, I. Martin, and P. Quinet, Lifetime calculations in Yb II, Journal of Physics B: Atomic, Molecular and Optical Physics **31**, 3321 (1998).

[26] V. A. Dzuba, V. V. Flambaum, and M. G. Kozlov, Combination of the many-body perturbation theory with the configuration-interaction method, Phys. Rev. A **54**, 3948 (1996).

[27] J. C. Berengut, D. Budker, C. Delaunay, V. V. Flambaum, C. Frugueule, E. Fuchs, C. Grojean, R. Harnik, R. Ozeri, G. Perez, and Y. Soreq, Probing new long-range interactions by isotope shift spectroscopy, Phys. Rev. Lett. **120**, 091801 (2018).

[28] V. A. Dzuba and A. Derevianko, Dynamic polarizabilities and related properties of clock states of the ytterbium atom, Journal of Physics B: Atomic, Molecular and Optical Physics **43**, 10.1088/0953-4075/43/7/074011 (2010), arXiv:0908.2278.

[29] M. S. Safronova, M. G. Kozlov, W. R. Johnson, and D. Jiang, Development of a configuration-interaction plus all-order method for atomic calculations, Phys. Rev. A **80**, 012516 (2009).

[30] C. Froese Fischer, G. Gaigalas, P. Jönsson, and J. Bieroń, GRASP2018 - a Fortran 95 version of the general relativistic atomic structure package, Computer Physics Communications **237**, 184 (2019).

[31] For The radial electron density $\rho_{\alpha}^{g,e}(r)$ for ground and excited states in transition α , $\int_0^{\infty} dr \rho_{\alpha}^{g,e}(r) = Z - I$ where I is the charge number of ion and $\rho_{\alpha}(r) = \rho_{\alpha}^e(r) - \rho_{\alpha}^g(r)$.

[32] J. Ekman, P. Jnsson, M. Godefroid, C. Naz, G. Gaigalas, and J. Biero, RIS4: A program for relativistic isotope shift calculations, Computer Physics Communications **235**, 433 (2019).

[33] E. C. Seltzer, K x-ray isotope shifts, Phys. Rev. **188**, 1916 (1969).

[34] S. A. Blundell, P. E. G. Baird, C. W. P. Palmer, D. N. Stacey, and G. K. Woodgate, A reformulation of the theory of field isotope shift in atoms, Journal of Physics B: Atomic and Molecular Physics **20**, 3663 (1987).

[35] K. Mikami, M. Tanaka, and Y. Yamamoto, Probing new intra-atomic force with isotope shifts, The European Physical Journal C **77**, 896 (2017).

[36] V. A. Dzuba, V. V. Flambaum, P. G. Silvestrov, and O. P. Sushkov, Relativistic many-body calculations in atoms and parity violation in caesium, Journal of Physics B: Atomic and Molecular Physics **18**, 597 (1985).

[37] E. Kahl and J. Berengut, ambit: A programme for high-precision relativistic atomic structure calculations, Computer Physics Communications **238**, 232 (2019).

[38] M. Roberts, P. Taylor, S. V. Gateva-Kostova, R. B. M. Clarke, W. R. C. Rowley, and P. Gill, Measurement of the $^2S_{1/2} - ^2D_{5/2}$ clock transition in a single $^{171}\text{Yb}^+$ ion, Phys. Rev. A **60**, 2867 (1999).

[39] C. Tamm, S. Weyers, B. Lipphardt, and E. Peik, Stray-field-induced quadrupole shift and absolute frequency of the 688-THz $^{171}\text{Yb}^+$ single-ion optical frequency standard, Phys. Rev. A **80**, 043403 (2009).

[40] S. Webster, R. Godun, S. King, G. Huang, B. Walton, V. Tsatourian, H. Margolis, S. Lea, and P. Gill, Frequency measurement of the $^2S_{1/2} - ^2D_{3/2}$ electric quadrupole transition in a single $^{171}\text{Yb}^+$ ion, IEEE Transactions on Ultrasonics, Ferroelectrics, and Frequency Control **57**, 592 (2010).

[41] G. Fricke and K. Heilig, Introduction, in *Nuclear Charge Radii*, Landolt-Börnstein - Group I Elementary Particles, Nuclei and Atoms, Vol. 20, edited by H. Schopper (Springer-Verlag, Berlin/Heidelberg, 2004) pp. 1–36.

[42] I. Angeli and K. Marinova, Table of experimental nuclear ground state charge radii: An update, Atomic Data and Nuclear Data Tables **99**, 69 (2013).

[43] W. Huang, G. Audi, M. Wang, F. G. Kondev, S. Naimi, and X. Xu, The AME2016 atomic mass evaluation (I). evaluation of input data; and adjustment procedures, Chinese Physics C **41**, 030002 (2017).

[44] M. Wang, G. Audi, F. G. Kondev, W. Huang, S. Naimi, and X. Xu, The AME2016 atomic mass evaluation (II). tables, graphs and references, Chinese Physics C **41**, 030003 (2017).

[45] A. Papouli, B. G. Carlsson, and J. Ekman, Effect of realistic nuclear charge distributions on isotope shifts and progress towards the extraction of higher-order nuclear radial moments, Phys. Rev. A **94**, 042502 (2016).

[46] M. Puchalski and K. Pachucki, Nuclear structure effects in the isotope shift with halo nuclei, Hyperfine Interactions **196**, 35 (2010).

[47] C. W. P. Palmer, Reformulation of the theory of the mass shift, Journal of Physics B: Atomic and Molecular Physics **20**, 5987 (1987).

[48] H. De Vries, C. De Jager, and C. De Vries, Nuclear charge-density-distribution parameters from elastic electron scattering, Atomic Data and Nuclear Data Tables **36**, 495 (1987).

[49] T. Sasanuma, *Electron Scattering from Deformed Heavy Nuclei*, Ph.D. thesis, Massachusetts Institute of Technology (1979).

[50] V. V. Flambaum, A. J. Geddes, and A. V. Viatkina, Isotope shift, nonlinearity of king plots, and the search for new particles, Phys. Rev. A **97**, 032510 (2018).